Liang *et al. Biomaterials Research* (2022) 26:32
https://doi.org/10.1186/s40824-022-00275-5

Biomaterials Research

REVIEW

Open Access

# Manganese-based hollow nanoplatforms for MR imaging-guided cancer therapies

Shuang Liang[1], Guangfu Liao[2*], Wenzhen Zhu[1*] and Li Zhang[3*]

## Abstract

Theranostic nanoplatforms integrating diagnostic and therapeutic functions have received considerable attention in the past decade. Among them, hollow manganese (Mn)-based nanoplatforms are superior since they combine the advantages of hollow structures and the intrinsic theranostic features of $Mn^{2+}$. Specifically, the hollow cavity can encapsulate a variety of small-molecule drugs, such as chemotherapeutic agents, photosensitizers and photothermal agents, for chemotherapy, photodynamic therapy (PDT) and photothermal therapy (PTT), respectively. After degradation in the tumor microenvironment (TME), the released $Mn^{2+}$ is able to act simultaneously as a magnetic resonance (MR) imaging contrast agent (CA) and as a Fenton-like agent for chemodynamic therapy (CDT). More importantly, synergistic treatment outcomes can be realized by reasonable and optimized design of the hollow nanosystems. This review summarizes various Mn-based hollow nanoplatforms, including hollow $Mn_xO_y$, hollow matrix-supported $Mn_xO_y$, hollow Mn-doped nanoparticles, hollow Mn complex-based nanoparticles, hollow Mn-cobalt (Co)-based nanoparticles, and hollow Mn-iron (Fe)-based nanoparticles, for MR imaging-guided cancer therapies. Finally, we discuss the potential obstacles and perspectives of these hollow Mn-based nanotheranostics for translational applications.

Graphical AbstractMn-based hollow nanoplatforms such as hollow $Mn_xO_y$ nanoparticles, hollow matrix-supported $Mn_xO_y$ nanoparticles, Mn-doped hollow nanoparticles, Mn complex-based hollow nanoparticles, hollow Mn-Co-based nanoparticles and hollow Mn-Fe-based nanoparticles show great promise in cancer theranostics.

*Correspondence: liaogf@mai2.sysu.edu.cn; zhuwenzhen8612@163.com; li.zhang@hit.edu.cn

[1] Department of Radiology, Tongji Hospital, Tongji Medical College, Huazhong University of Science and Technology, Wuhan 430030, China
[2] Engineering Research Center of Nano-Geomaterials of Ministry of Education, China University of Geosciences, Wuhan 430074, China
[3] School of Science, Harbin Institute of Technology (Shenzhen), Shenzhen 518055, China

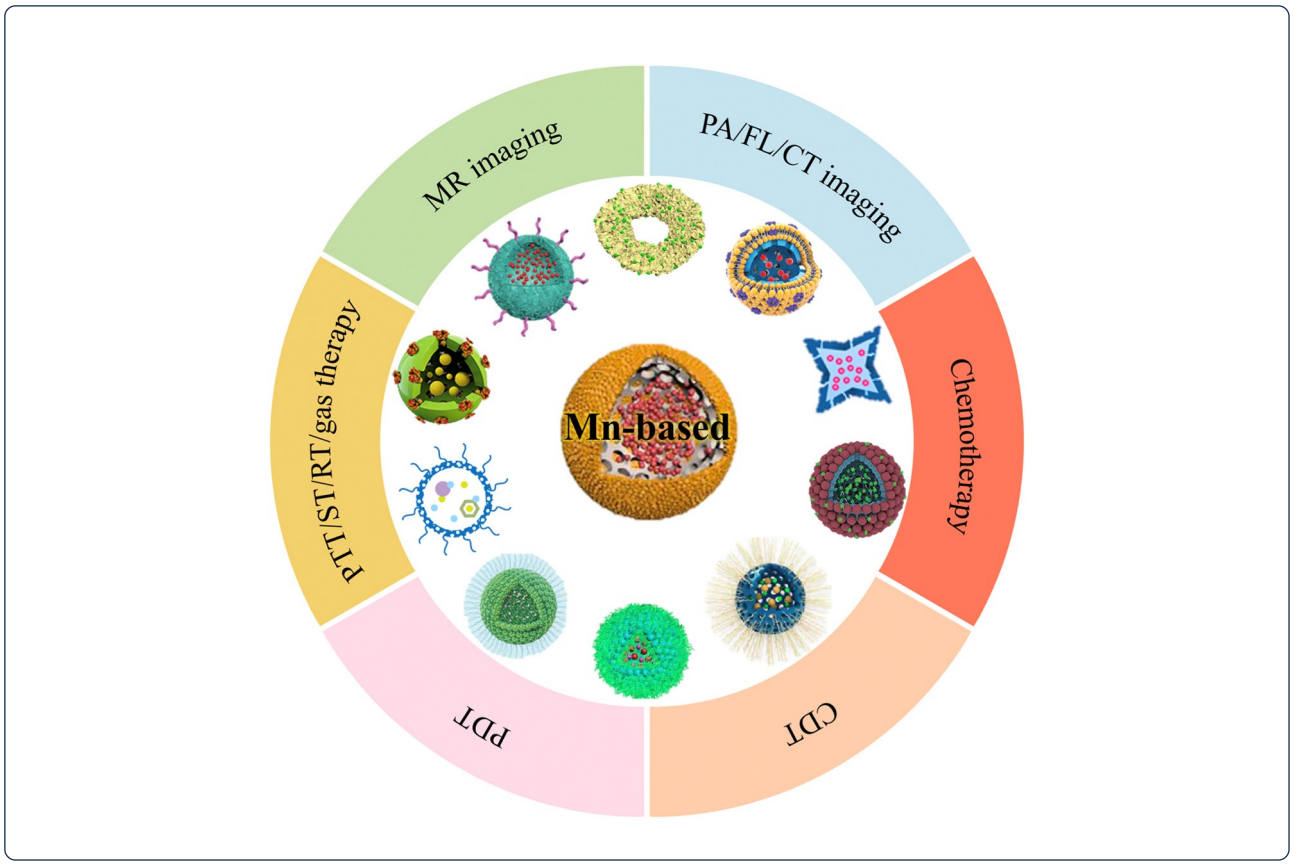


## Introduction

Cancer has always been considered one of the deadliest diseases that threatens human life, and the number of cases is increasing year by year [1–4]. Theranostic nanoplatforms that integrate diagnostic and therapeutic units have proven to be significant for cancer treatment in the past decade [5–7]. Among the imaging approaches in clinical use, magnetic resonance (MR) imaging, developed based on the nuclear magnetic resonance (NMR) principle, is more attractive due to its non-invasiveness and potent spatial resolution, especially for soft tissue detection [8–10]. With the rapid advances in nanotechnology, a variety of MR imaging contrast agents (CAs) have been utilized for improving the resolution and sensitivity during scans [11, 12]. To date, CAs have been involved in more than 40% of MR imaging examinations [13]. Generally, MR imaging CAs can be divided into two major categories based on their relaxation processes, i.e., $T_1$ and $T_2$ CAs. $T_1$ CAs are able to shorten the longitudinal relaxation time of the surrounding water protons and increase the signal intensity of $T_1$-weighted images, while $T_2$ CAs shorten the transverse relaxation time of the surrounding water protons and reduce the signal intensity of $T_2$-weighted images [14–17]. Paramagnetic $Gd^{3+}$ complexes and iron oxide (IO) nanoparticles are representative commercial $T_1$ and $T_2$ CAs, which are beneficial to the detection of tumors [18–20].

Nevertheless, the widespread clinical application of $T_2$-weighted MR imaging is hampered by confusion between the negative contrasts generated and other pathological environments, which limits diagnostic accuracy [21]. In addition, IO nanoparticles with high susceptibility distort the circumjacent magnetic field and cause blurred images [22, 23]. Taking all these factors into consideration, $T_1$ CAs are more promising than $T_2$ CAs for precise and high-resolution imaging [24]. However, the premature leakage of $Gd^{3+}$ may cause systemic toxicity, and $Gd^{3+}$ complex CAs often suffer from short blood circulation as well as nonspecific distribution [25–27]. The development of new positive CAs with all the above-mentioned issues resolved is urgently needed. Over the past 10 years, Mn-based nanomaterials such as $Mn_xO_y$ and MnS have drawn increasing interest in biomedical applications [28–32]. These nanoplatforms with passive or active targeting ability are capable of selectively accumulating at the tumor site, which leads to highly effective MR imaging after degradation in the tumor microenvironment (TME) [33, 34]. In addition,

Mn is one of the necessary elements in human bodies for metabolism, and its uptake and excretion can be efficiently controlled by biological systems, resulting in low toxicity and high biosafety [35–37]. Notably, single-modal imaging with insufficient diagnostic information sometimes cannot meet the high requirements of modern medicine [38–41]. Therefore, there is increasing interest in the exploration of multi-modal imaging CAs. For instance, dual-modal $T_1$- and $T_2$-weighted MR imaging that integrates both positive and negative CAs merits can allow enhanced diagnosis by highlighting the anatomical details in MR images [42–44]. Moreover, the combination of MR imaging with fluorescence (FL) imaging is capable of providing complementary information, as FL imaging compensates for the inferior sensitivity of MR imaging, and in turn, MR imaging remedies the weak spatial resolution and tissue penetration of FL imaging [45–47]. Furthermore, photoacoustic (PA) imaging is a newly developed modality that incorporates the advantages of both optical and ultrasonic imaging, and much attention has been given to constructing various CAs for dual-modal MR/PA imaging [48–50].

To overcome the side effects and simultaneously improve the therapeutic outcome of conventional chemotherapy and radiotherapy (RT), various smart drug delivery systems (DDSs), especially hollow DDSs, have been explored [51–55]. The preparation strategies for high-quality hollow DDSs can be divided into two main categories: (1) sacrificial template-based methods, which exploit a variety of removable nanoparticles as hard templates (e.g., silica, polystyrene and metal-organic frameworks (MOFs)) [56–61] or soft templates (e.g., Pluronic F127/TMB and gas bubbles) [62, 63]; and (2) self-templating methods, which employ the transformation of self-generated internal solid nanoparticles to hollow structures during chemical reactions [64–68]. The former approach has been widely applied to produce various hollow nanoparticles with uniform morphology and a tuneable diameter and shell thickness, such as hollow $MnO_2$ [69, 70], hollow polydopamine (PDA) [71, 72], hollow carbon [73, 74] and hollow mesoporous organosilica nanoparticles (HMON) [75, 76], whereas the relatively recently developed latter approach is considered superior owing to the simple synthetic procedures and reduced formation of chemical waste [77]. For the self-templating method, the nanoscale Kirkendall effect, galvanic replacement reaction and Ostwald ripening process are often used to prepare hollow $Cu_7S_4$ nanocrystals [78], Au−Ag@Au hollow nanostructures [79] and hollow cuprous oxide@nitrogen-doped carbon dual-shell structures [80], respectively. More importantly, DDSs with responsive diagnostic and therapeutic functions can assist in tumor detection as well as monitor drug release and treatment processes within a certain TME [60, 81]. Among the hollow TME-responsive DDSs, Mn-based nanoplatforms display tremendous promise in bioimaging, drug delivery and tumor therapy owing to their good biocompatibility, unique hollow structures and excellent physical/chemical performances [69, 82]. For instance, hollow $MnO_2$ nanoparticles can rapidly respond to the TME, catalyzing intracellular hydrogen peroxide ($H_2O_2$) to produce $O_2$ and concurrently depleting the overexpressed glutathione (GSH) [33, 83]. The generated $O_2$ benefits additional treatment modalities, such as chemotherapy [84], RT [85], photodynamic therapy (PDT) [84], sonodynamic therapy (SDT) [86] and starvation therapy (ST) [87], while the consumption of GSH leads to redox imbalance and further improves the curative effects of reactive oxygen species (ROS)-mediated therapies [88]. Moreover, the released $Mn^{2+}$ can serve as a good Fenton-like agent for chemodynamic therapy (CDT) and simultaneously as a CA for $T_1$-weighted MR imaging [89, 90]. Furthermore, due to the degradation of hollow structures in the TME, the loaded cargoes can be released to perform diverse treatments under the guidance of MR imaging [69, 82, 91]. By reasonable and optimal design, such hollow nanosystems are also expected to realize synergistic diagnostic and therapeutic outcomes [81, 92].

This review summarizes the recent progress in Mn-based hollow nanoplatforms for MR imaging-guided cancer therapies, with several sections presented according to the different nanostructures. In each chapter, the basic introduction of the corresponding hollow materials is first given, followed by a detailed summary of the applications including MR, PA, FL and computer tomography (CT) imaging as well as chemotherapy, CDT, PDT, photothermal therapy (PTT), ST, RT and gas therapy. In addition to single-magnetic-core Mn-based hollow nanoplatforms including hollow $Mn_xO_y$, hollow matrix-supported $Mn_xO_y$, Mn-doping hollow nanoparticles and Mn complex-based hollow nanoparticles, dual-magnetic-core hollow Mn-Cobalt (Co)-based nanoparticles and hollow Mn-iron (Fe)-based nanoparticles are also introduced (Scheme 1). Finally, the potential obstacles and prospects involved in the translational application of these hollow Mn-based nanotheranostics are discussed.

## Single-magnetic-core Mn-based hollow nanoplatforms for MR imaging-guided cancer therapies

### *Hollow $Mn_xO_y$ alone*

There are several categories of hollow $Mn_xO_y$ nanomaterials, including $HMnO_2$ [93], HMnO [94], $HMn_3O_4$ [95], and $HMn_2O_3$ [96]. $HMnO_2$ is the most popular for cancer theranostics. The synthesis of $HMnO_2$ often involves a

sacrificial template-based method, which uses solid silica nanoparticles and polymer nanoparticles as substrates. After dissolution of the inner cores, the resultant cavity can be used to carry a variety of small molecule drugs, such as chemotherapeutic agents, photosensitizers, and photothermal agents. For chemotherapy, PDT and PTT, respectively.

For example, Wang et al. [81] utilized poly(lactic-co-glycolic acid) (PLGA) nanoparticles as a template to prepare $HMnO_2$, which further served as a nanocarrier to deliver bufalin to the tumor site with the help of a platelet membrane (PLTM) (Fig. 1). Platelet modification was able to prevent the phagocytic uptake of the as-prepared PLTM-$HMnO_2$@Bu nanoparticles by macrophages due to the self-recognition signals sent by the CD47 membrane protein. In addition, the upregulation of P-selectin on the PLTM facilitated the attachment of platelets to tumor cells through specific binding to the overexpressed CD44 receptors. The $HMnO_2$ nanoparticles were rapidly degraded at acidic pH and at high levels of GSH, promoting bufalin (Bu) release and the simultaneous formation of $Mn^{2+}$. The resultant $Mn^{2+}$ further catalyzed the conversion of endogenous $H_2O_2$ to hydroxyl radicals (•OH) for CDT. Tumor growth was effectively inhibited by PLTM-$HMnO_2$@Bu nanoparticles due to the combination of CDT and chemotherapy. Additionally, the off-to-on TME-responsive MR imaging performance was examined, and the signal intensities of the tumor site displayed a gradual increase with time. These results revealed that PLTM-$HMnO_2$@Bu was very promising for targeted MR imaging guidance and enhanced cancer treatment.

To realize more accurate cancer imaging and efficient therapy, Wu et al. [93] reported a multifunctional nanotheranostic (H-$MnO_2$/DOX/BPQDs), in which black phosphorus quantum dots (BPQDs) served as both the photosensitizer and photothermal agent. Briefly, monodispersed $SiO_2$ nanoparticles, the hard template, were dissolved after in situ decoration of the mesoporous $MnO_2$ layer on their surface. Then, the obtained H-$MnO_2$ was sequentially modified with poly(allylamine hydrochloride) (PAH) and poly(acrylic acid) (PAA). Subsequently, BPQDs-PEG-$NH_2$ (PEG for polyethylene glycol) was covalently grafted onto H-$MnO_2$-PAH-PAA by a carbodiimide cross-linking reaction, followed by loading with doxorubicin (DOX) (Fig. 2a). As shown in Fig. 2b, the as-prepared monodispersed H-$MnO_2$/DOX/BPQDs were hollow and spherical in shape with an average particle size of ~ 300 nm. The decomposition behaviour was then investigated by incubating H-$MnO_2$/DOX/BPQDs in PBS solution at pH 7.4 and pH 5.0. The morphology in the pH 7.4 groups showed no significant changes, while obvious collapses were found in the

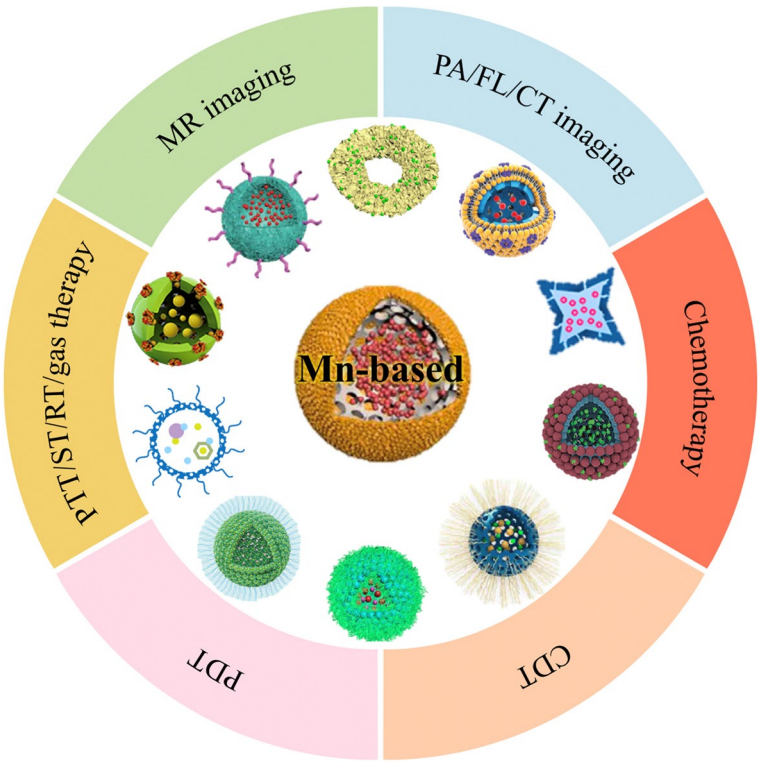


**Scheme 1** Schematic illustration of various Mn-based hollow nanoplatforms for cancer theranostics.

pH 5.0 groups, indicating the great potential of H-$MnO_2$ as a pH-sensitive nanocarrier (Fig. 2c). Upon 630 nm laser irradiation, the absorbance of the H-$MnO_2$/DOX/BPQDs and 1,3-diphenylisobenzofuran (DPBF) mixture showed a decrease over time, which indicated singlet oxygen ($^1O_2$) generation due to the presence of BPQDs (Fig. 2d). Moreover, the photothermal performance of the H-$MnO_2$/DOX/BPQDs was also demonstrated, as revealed by the temperature elevation when exposed to an 808 nm laser (Fig. 2e). Furthermore, the H-$MnO_2$/DOX/BPQDs displayed typical catalase (CAT)-like property, providing sufficient $O_2$ for enhanced PDT in the $H_2O_2$ solution (Fig. 2f). Consequently, the H-$MnO_2$/DOX/BPQDs + L630 group showed the strongest cellular green fluorescence of ROS. Taking all these features together, the $MnO_2$/DOX/BPQDs was expected to be an ideal therapeutic agent. As shown in Fig. 2h, only 28.63% of the HepG2 cells survived after treatment with H-$MnO_2$/DOX/BPQDs + L630 + L808 when the concentration was 200 μg $mL^{-1}$, revealing that the combined chemophototherapy was much more effective than PDT, PTT or chemotherapy alone. Consistently, a significantly higher tumor growth inhibition rate was obtained in the H-$MnO_2$/DOX/BPQDs + L630 + L808 group (Fig. 2i). In addition, the strongest fluorescence intensity of DOX in the tumor was observed at 12 h post-injection due to the EPR effect, and the $T_1$-MR signals displayed a 4-fold increase after injection for 24 h (Fig. 2j, k). The H-$MnO_2$/DOX/BPQDs + L630 + L808 with dual-modal MR/FL imaging and synergistic chemotherapy/PDT/PTT capabilities showed great promise for improving diagnostic accuracy and therapeutic outcomes.

Zhu et al. [97] constructed cancer cell vesicle (CV)-coated $HMnO_2$ nanoparticles with camptothecin (CPT) encapsulated (denoted CMC) to boost RT, which was the first example of utilizing $HMnO_2$ in RT sensitization (Fig. 3). The cancer cell membrane coating endowed the nanoparticles with prolonged blood circulation and targeting ability. After cellular uptake, $HMnO_2$ reacted with the acidic $H_2O_2$ to generate large amounts of $O_2$ and release CPT and $Mn^{2+}$ ions. The antitumor mechanism

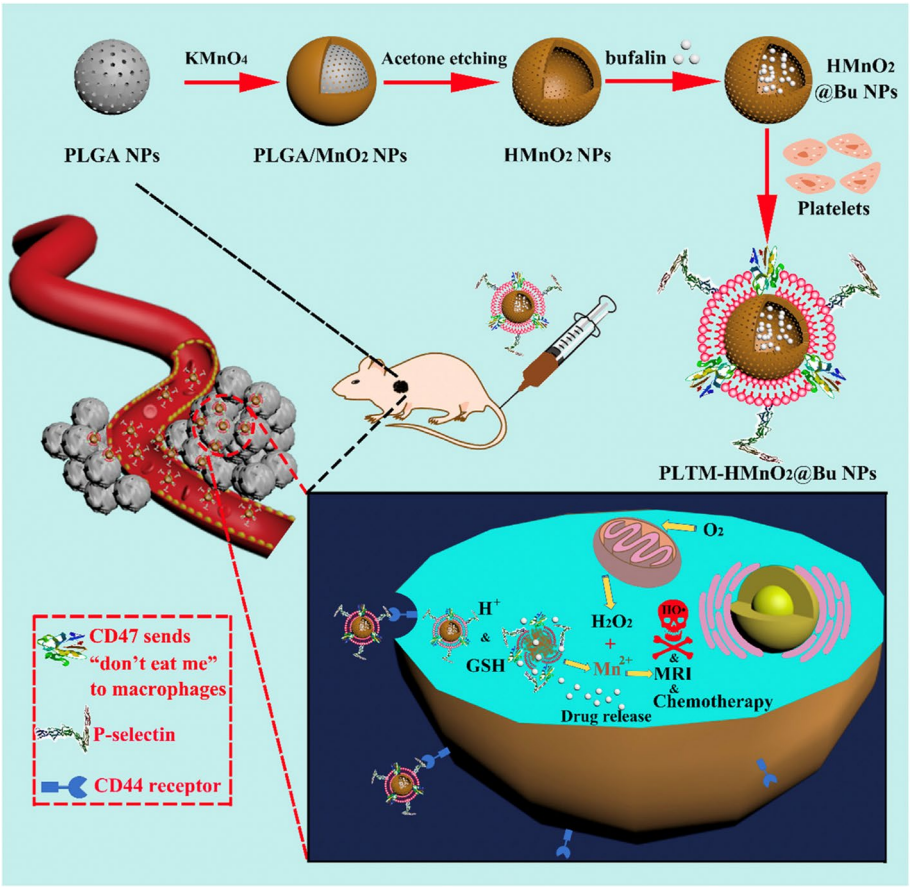


**Fig. 1** Illustration of the preparation of PLTM-H$MnO_2$@Bu NPs and in vivo MR iamging-monitored targeted chemo-chemodynamic combined therapy. Reproduced with permission from Ref. [81]. Copyright 2020, Elsevier Inc.

mainly involved the following: (1) $O_2$ production was capable of suppressing hypoxia inducible factor-1 (HIF-1) expression, thus improving the RT sensitivity of the cells, and (2) a low dose of CPT blocked the cell cycle in the S-phase (radiosensitive phase), which further promoted radiation-induced damage. Additionally, the released $Mn^{2+}$ acted as a $T_1$-weighted MR imaging CA to identify the tumor sites. This work offeres a new idea for designing RT sensitization systems.

As another type of $Mn_xO_y$, MnO is also of widespread interest for cancer imaging and therapy. For example, Wei et al. [98] reported novel octapod-shaped hollow porous manganese(II) oxide (HPMO) nanoparticles with small particle sizes for stimuli-responsive $T_1$-weighted MR imaging and targeted cargo delivery. The zwitterionic dopamine sulfonate (ZDS)-modified HPMO nanoparticles were able to be a versatile platform for loading organic dyes or chemotherapeutic drugs. Upon encountering the TME, especially lysosomes, the as-prepared DOX@HPMO could be decomposed into $Mn^{2+}$ ions with cargoes subsequently released. The liberated DOX then recovered its fluorescence that was previously quenched by HPMO, visualizing the release process. Meanwhile, $Mn^{2+}$ could be used for $T_1$-weighted MR imaging, which also enabled monitoring the in vivo DOX release in real time. Thanks to the pH-sensitive dual-modal imaging modalities and site-specific drug delivery, this versatile and intelligent nanoplatform was beneficial for accurate cancer diagnosis and effective therapy.

#### *Hollow matrix-supported $Mn_xO_y$*

$MnO_2$ can also be engineered on different hollow matrices, and the intrinsic performances of those matrices together with the features of $MnO_2$ are expected to bring about a greater breakthrough in cancer theranostics [99, 100]. As a proof of concept, a hollow matrix possessing photothermal effect or Fenton-like catalytic performance could be used for PTT or CDT, cooperating with the therapeutic features of $MnO_2$ to further improve the treatment outcomes [101].

PDA has become a new class of biomaterials for biomedical applications owing to its various biological functions and unique chemical properties [102–104]. In addition to being a good photothermal agent for photoacoustic (PA) imaging/PTT, the plentiful aromatic rings and functional groups of PDA make it possible to load chemical drugs and facilitate surface modification as well as the chelation of diverse metal ions for multi-modal imaging [105–107]. Hollow-structured PDA (HPDA) is regarded as an excellent nanocarrier due to its large cavity and biodegradability in the acidic TME [108, 109]. Wang et al. [71] fabricated a novel cancer-specific and TME-responsive nanoplatform (HPDA@$MnO_2$@RGD@Ce6/DOX, denoted as HPMRCD) for FL/MR imaging and combined chemotherapy/PDT. The HPMRCD was enriched in the tumor site as a result of the targeting ability of arginine-glycine-aspartic acid (RGD) and then instantly decomposed in the acidic high-$H_2O_2$ TME. The generated $O_2$ could alleviate tumor hypoxia, while the released $Mn^{2+}$ ions led to greatly improved contrast of $T_1$-weighted MR imaging. Simultaneously, the degradation of the inner HPDA resulted in the effective release of loaded DOX and Ce6, thus remarkably inhibiting tumor growth by employing dual-modal chemotherapy and PDT. Interestingly, the in vivo fluorescence imaging of Ce6 was also able to locate the tumor site and guide the therapeutic process. This work provides a promising method for chemotherapy/PDT using a self-enhanced theranostic nanoplatform.

The strong surface plasmon resonance (SPR) endows noble metal nanoparticles with prominent optical and photothermal performances, including a high absorption cross-section and superior photothermal conversion efficiency in the NIR biowindow, resulting in extensive application prospects in bioimaging and PTT [110–112]. Based on hollow Au/Ag alloy nanoparticles, Wu et al. [113] fabricated a versatile nanoplatform

(See figure on next page.)

**Fig. 2** **a** Schematic illustration of nanoprobe H-$MnO_2$/DOX/BPQDs synthesis route and its applications for hypoxic cancer multimodal imaging and synergistic therapy, involving MR/FL imaging and enhanced PDT/PTT/chemotherapy. **b** TEM photos of H-$MnO_2$/DOX/BPQDs incubated with pH 7.4 (physiological condition) and pH 5.5 buffer (tumor environment) for different times. **c** Percentages of released DOX from H-$MnO_2$/DOX/BPQDs over time in the PBS at different pH values (7.4, 6.5, and 5.5). Data were presented as means ± standard deviation (s.d.) ($n = 3$). **d** The $^1O_2$ generation ability of H-$MnO_2$/DOX/BPQDs in air with 1,3-diphenylisobenzofuran (DPBF). **e** Photothermal heating curves of the H-$MnO_2$/DOX/BPQDs aqueous dispersions with different concentrations (0, 0.1, and 0.2 mg $mL^{-1}$) and H-$MnO_2$/DOX upon 808 nm laser irradiation (1.0 W $cm^{-2}$). **f** The dissolved $O_2$ concentration in 100 μm $H_2O_2$ solutions after treated with different concentrations of H-$MnO_2$/DOX/BPQDs (0, 0.1, and 0.2 mg $mL^{-1}$). **g** Confocal images of intracellular ROS generation in HepG2 cells treated with Control + L630 (I), H-$MnO_2$/DOX + L630 (II), BPQDs-PEG-$NH_2$ + L630 (III), and H-$MnO_2$/DOX/BPQDs + L630 (IV), as detected with 2′,7′-dichlorodihydrofluorescein diacetate (DCFH-DA). **h** Cell viability of HepG2 cells after treatment with various concentrations of H-$MnO_2$/DOX/BPQDs under 630 and/or 808 nm laser irradiation. **i** The photographs of tumor dissection of different treatment groups obtained at 15 days. **j** In vivo fluorescence images of HepG2 tumor-bearing mice at different time points after systemic administration of nanoprobe H-$MnO_2$/DOX/BPQDs ($MnO_2$: 10 mg $kg^{-1}$; DOX: 4.5 mg $kg^{-1}$; BPQDs: 10 mg $kg^{-1}$) via tail vein injection. **k** In vivo $T_1$-MR images of a mouse taken before and after systemic administration of H-$MnO_2$/DOX/BPQDs at 24 h. Reproduced with permission from Ref. [93]. Copyright 2021, Wiley-VCH Verlag GmbH & Co. KGaA, Weinheim

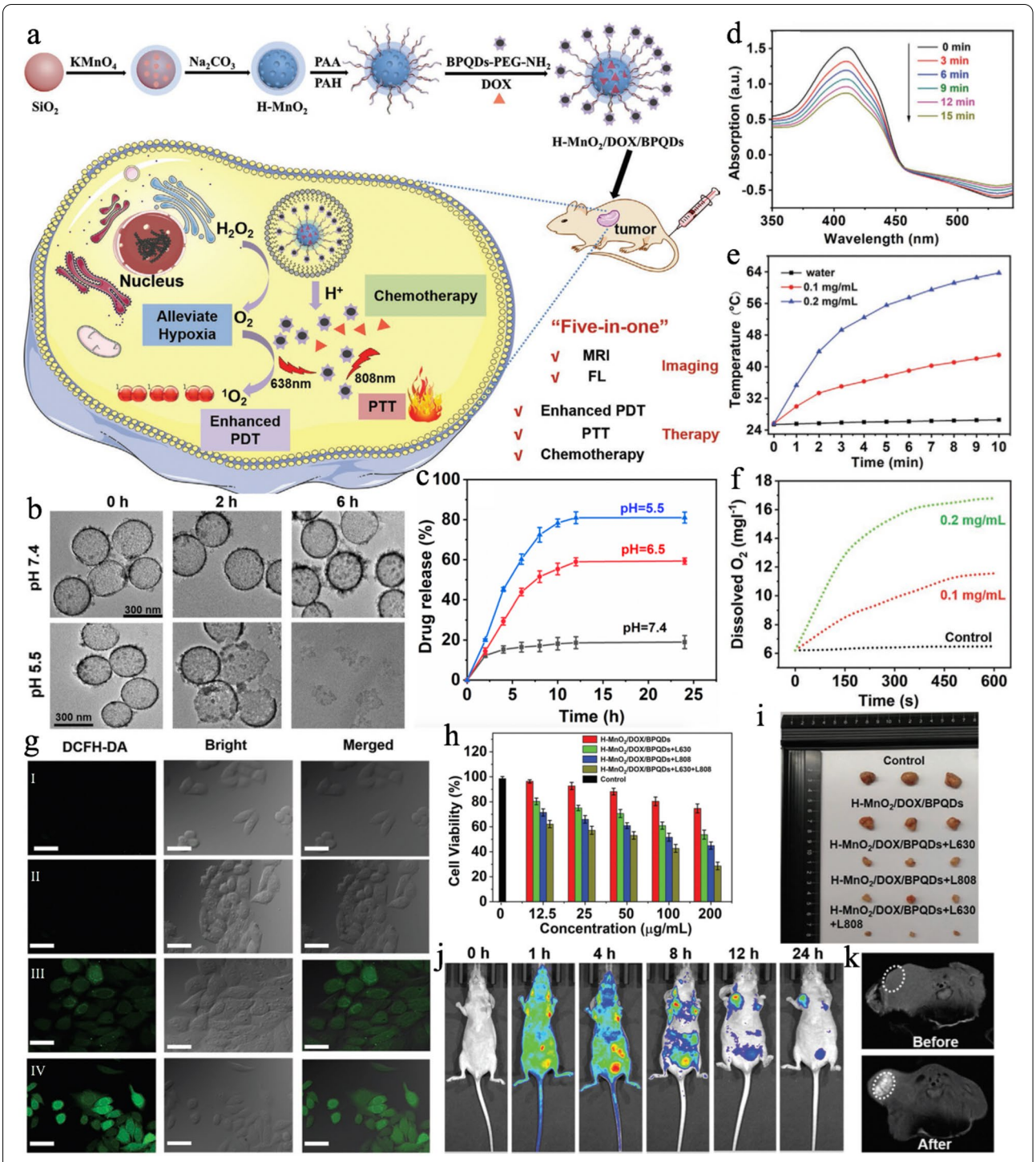


**Fig. 2** (See legend on previous page.)

(Au/Ag-$MnO_2$-PEG/Ce6, denoted as AAM-Ce6) with $MnO_2$ and PEG functionalized as well as Ce6 loaded. The AAM showed intensive optical absorption in the NIR-II region and possessed remarkable photothermal effects (PCE = 52.5% at 1064 nm) for NIR-II PTT and PA imaging. After AAM-Ce6 reached the tumor site, the outer $MnO_2$ nanoparticles quickly responded to the TME, producing a large amount of $O_2$ to promote PDT and massive amounts of $Mn^{2+}$ ions to turn on MR imaging. Meanwhile, the released Ce6 also provided decent

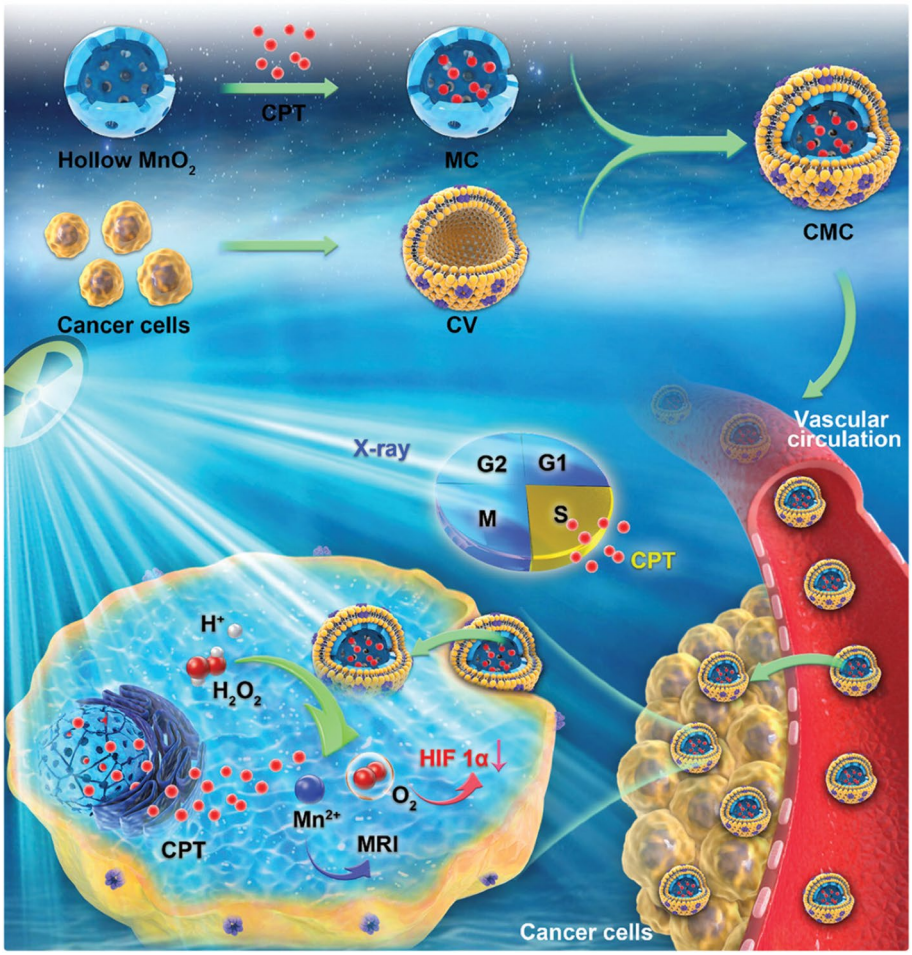


**Fig. 3** Schematic illustration of the biomimetic nanozyme/CPT hybrid system for synergistically enhanced RT. Reproduced with permission from Ref. [97]. Copyright 2020, The Royal Society of Chemistry

FL imaging performance and converted $O_2$ to $^1O_2$ for enhanced PDT under a 660 nm laser. When concurrently treated with 1064 nm and 660 nm lasers, AAM-Ce6 exhibited synergistically improved therapeutic efficacy, which was much better than PTT or PDT alone.

MOFs consisting of metal ions and organic ligands hold great potential for theranostic applications due to their channels/pores and active metal ions [114, 115]. In addition, MOFs are also selected as templates or substrates to obtain multifunctionality [87, 116]. Utilizing a mixed-metal Cu/Zn-MOF as the precursor, Cheng et al. [92] proposed a novel hollow nanoplatform (ICG@Mn/Cu/Zn-MOF@$MnO_2$) for triple-modal imaging and synergistic PTT/PDT/CDT. The synthetic process of ICG@Mn/Cu/Zn-MOF@$MnO_2$ is illustrated in Fig. 4a. Briefly, Cu/Zn-MOF was first prepared and underwent the Ostwald ripening process to obtain a hollow porous structure with coexisting $Cu^+$ and $Cu^{2+}$. Subsequently, the manganese(II) acetylacetonate ($Mn(aac)_2$) solution was added under heating treatment to introduce $Mn^{2+}$ and $MnO_2$, followed by ICG encapsulation. The aggregation of ICG in ICG@Mn/Cu/Zn-MOF@$MnO_2$ allowed good photothermal imaging (PTI) and PTT upon exposure to laser irradiation. Along with the degradation of ICG@Mn/Cu/Zn-MOF@$MnO_2$, ICG was gradually released, and its FL imaging and PDT capacities were recovered. Moreover, the in situ catalytic decomposition of intratumoral $H_2O_2$ led to massive $O_2$ production, enhancing ICG-induced PDT. Furthermore, the $Cu^+$ and $Mn^{2+}$ ions were ideal Fenton-like agents that could intensively catalyze $H_2O_2$ to generate highly active and cytotoxic •OH for improved CDT with the assistance of hyperthermia from PTT. Notably, these ROS-mediated therapies were further improved due to the depletion of GSH by $Cu^{2+}$ and $MnO_2$. In addition, the TME-activated MR imaging capability was also evaluated for therapeutic guidance. This novel antitumor paradigm achieved highly efficient

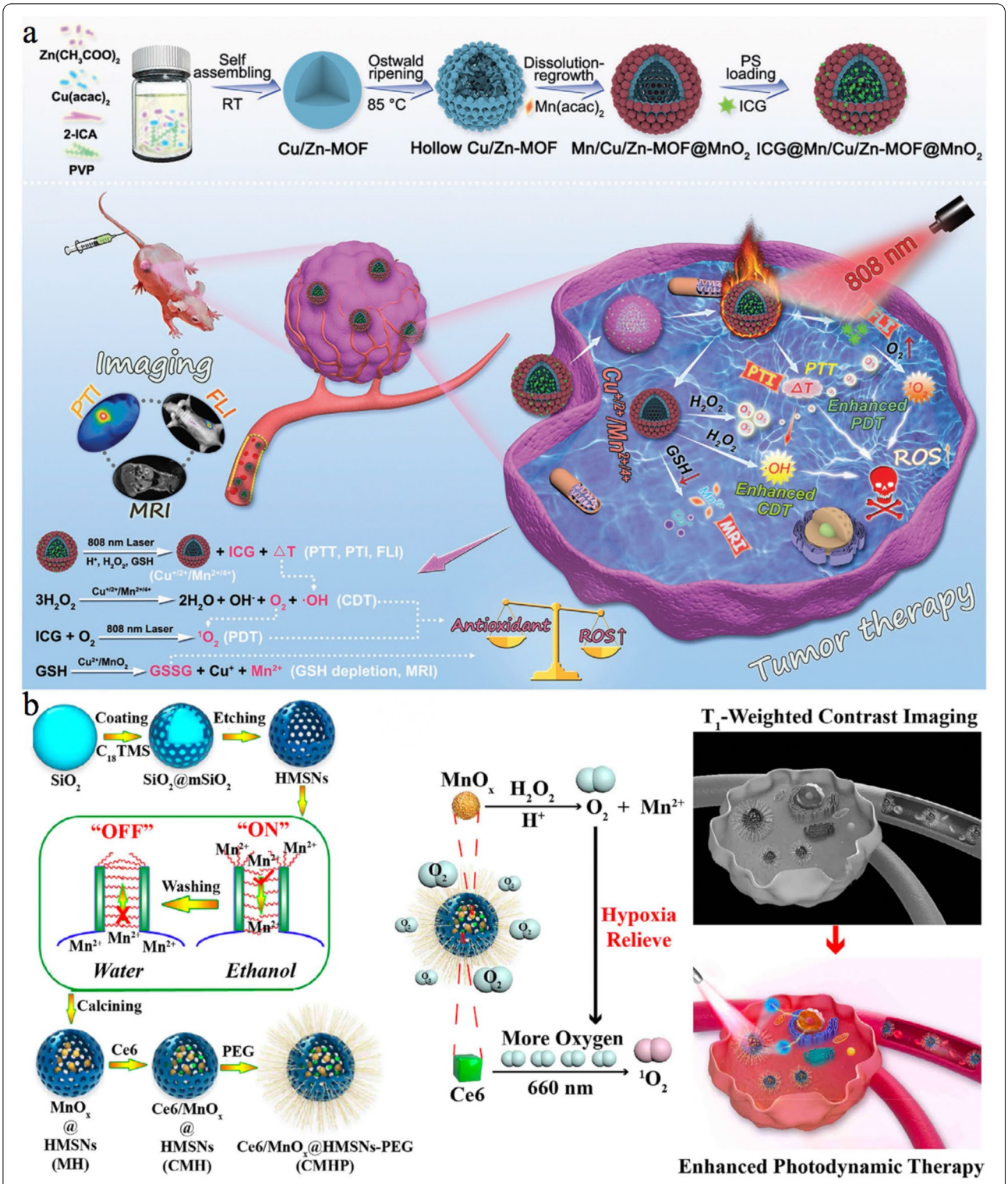


**Fig. 4** **a** Schematic illustration for the fabrication of ICG@Mn/Cu/Zn-MOF@$MnO_2$ and the scheme of therapeutic mechanism for PTI/FL/MR imaging guided ROS-augmented synergistic PTT/PDT/CDT. Reproduced with permission from Ref. [92]. Copyright 2021, Wiley-VCH Verlag GmbH & Co. KGaA, Weinheim. **b** Diagrams of the synthetic protocol and MR imaging-guided PDT of CMHP nanoreactors including detailed synthetic steps of site-specific loading both $MnO_x$ and Ce6 into HMSNs based on on/off state of mesoporous channels and schematic diagram of theranostic functions of CMHP nanoreactors, i.e., MR imaging-guided and oxygen generation to improve PDT efficacy. Reproduced with permission from Ref. [117]. Copyright 2020, Elsevier Inc.

treatment and caused insignificant damage to normal tissues, realizing the integration of multi-functions onto hollow nanoplatforms for improved diagnosis and therapies via synergistic manners.

Based on the above, most studies have focused on decorating $Mn_xO_y$ on the outside of hollow substrates, but it is uncommon to see $Mn_xO_y$ encapsulated inside the cavity of the matrix. For the first time, Du et al. [117] reported a smart on/off switching method to load both $MnO_x$ and Ce6 into hollow mesoporous silica nanoparticle (HMSN) (denoted CMH) (Fig. 4b). The key to this novel system was the utilization of the surfactant C18TMS, a mesostructured-directing agent possessing diverse solubilities in various solvents. When C18TMS-containing HMSNs were dispersed in ethanol, C18TMS was dissolved to open the mesoporous channel (on state); thus, the Mn precursor could easily enter the hollow structures. In contrast, C18TMS showed hydrophobicity in water, which closed the mesoporous channel (off state) and confined the Mn precursor inside. The C18TMS was removed after calcination with $MnO_x$ generated, and the channel opened; thus, Ce6 could also be loaded. This new method guaranteed the precise encapsulation of both Mn and Ce6, in which $MnO_x$ was capable of decomposing endogenous $H_2O_2$ to produce $O_2$ and $Mn^{2+}$ to improve the efficiency of Ce6-induced PDT and $T_1$-weighted MR imaging, respectively. This work introduces a novel strategy that enabled confined nanoparticles to grow within hollow structures, paving a new way to design multifunctional nanoplatforms for different biomedical applications.

### *Mn-doped hollow nanoparticles*

Metal-doped nanoparticles, another unique type of nanomaterial, are recommended for application in biomedical applications because of their low self-toxicity [118–121]. Doping with Mn enhances the magnetic and catalytic properties of substrates that are in favor of bioimaging and cancer therapy. For example, Mn-doped $ZnO_2$ endowed the nanoplatform with activatable MR imaging

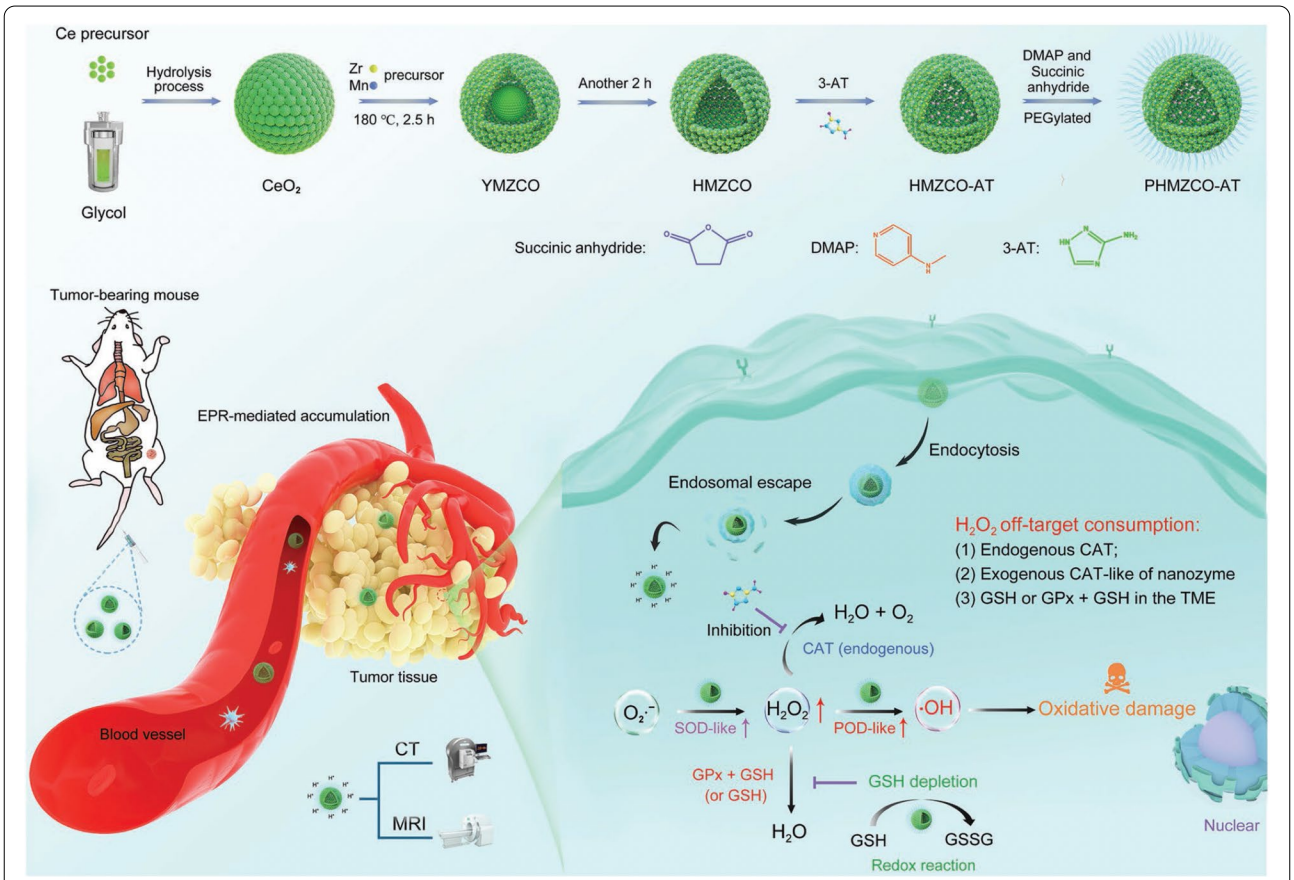


**Fig. 5** Design, fabrication, and catalysis-based therapeutic schemes of PHMZCO-AT tandem nanozyme including synthetic procedure of PHMZCO-AT nanozymes with hollow or yolk-shell structure and scheme of catalytic $H_2O_2$ generation, inhibition of the off-target $H_2O_2$ consumption, and continuous •OH production for intensive NCDT by PHMZCO-AT nanozymes. Reproduced with permission from Ref. [126]. Copyright 2022, Wiley-VCH Verlag GmbH & Co. KGaA, Weinheim

performance, which could be used to monitor acid-induced $ZnO_2$ dissociation and the subsequent treatment process [122]. Moreover, Tian et al. [123] found that Mn incorporation could easily alter the $Fe_2P$ electron density, significantly promoting Fe catalytic activity with the generation of 4-fold •OH. Furthermore, Fu et al. [124] reported Mn-doped ZrMOF nanocubes displaying highly effective combined microwave dynamic and thermal cancer therapies.

Regarding Mn-doped hollow nanoparticles, Zou et al. [125] developed a pH/GSH dual-responsive theranostic nanoplatform (DOX-Mn-ZGOCS-PEG) based on Mn-doped hollow silica with ultrasmall persistent phosphor (ZGOCS)/DOX co-loaded and PEG modified. In this design, the −Mn−O− bonds were intensively dissociated under acidic and reducing TME, leading to the gradual biodegradation of DOX-Mn-ZGOCS-PEG and massive DOX release. Meanwhile, the resultant $Mn^{2+}$ was able to greatly heighten the contrast of $T_1$-weighted MR imaging. More importantly, the previously quenched persistent luminescence (PL) of ZGOCS was recovered for autofluorescence-free diagnosis as DOX-Mn-ZGOCS-PEG disintegrated. In vivo experiments showed that DOX-Mn-ZGOCS-PEG displayed an impressive tumor inhibition rate with negligible side effects and good biodegradability. Together, DOX-Mn-ZGOCS-PEG could realize tumor-targeted boosted chemotherapy under the guidance of TME-activated MR/NIR-PL dual-modal imaging, holding enormous translational potential in accurate cancer diagnosis and therapy.

Dong et al. [126] reported a hollow mesoporous tandem nanozyme (denoted PHMZCO-AT) for $T_1$-weighted MR/CT imaging-guided highly efficient catalytic treatment (Fig. 5). By co-doping $Mn^{4+}/Zr^{2+}$ into $CeO_2$ nanoparticles, a hollow-structured HMZCO was formed based on the Kirkendall effect. Subsequently, 3-amino-1,2,4-triazole (3-AT) was encapsulated into the interior cavity, and PEG was functionalized on the surface to obtain PHMZCO-AT. Compared to the pure $CeO_2$ nanoparticles, the as-prepared PHMZCO-AT nanozyme possessed enhanced superoxide dismutase (SOD)- and peroxidase (POD)-like activities under mildly acidic condition because the variable-valence Mn ions doping triggered intermetallic charge transfer and thus accelerated the $Ce^{4+}/Ce^{3+}$ redox cycles. In addition, the loaded AT in PHMZCO-AT acted as an endogenous CAT inhibitor and weakened the catalytic decomposition of $H_2O_2$, as evidenced by the elevated Michaelis–Menten constants ($K_m = 180.67$ mM) and reduced maximum reaction rate ($V_{max} = 0.12\ mg\ L^{-1}\ min^{-1}$) at pH 5.5, while the $K_m$ and $V_{max}$ of pure $CeO_2$ at pH 7.4 were 77.64 mM and $0.34\ mg\ L^{-1}\ min^{-1}$, respectively. When PHMZCO-AT reached the TME, the endogenous superoxide anion ($O_2•^-$) was first converted to $H_2O_2$ due to the SOD-like activity. Then, the POD-like activity of PHMZCO-AT allowed the generation of massive amounts of highly toxic •OH from the elevated $H_2O_2$. Interestingly, the $H_2O_2$ level was further enhanced as a result of the CAT-suppressive feature of the 3-AT molecule and GSH-depleting behavior of PHMZCO-AT, boosting the production of •OH for effective oxidative damage, and a superior tumor inhibition rate (81.9%) was achieved on 4T1 tumor xenografts. In addition, the paramagnetic property of $Mn^{2+}$ and Zr with high X-ray damping capacity enabled PHMZCO-AT to serve as both a $T_1$-weighted MR imaging and a CT imaging CA. This work provides a general strategy to construct advanced nanozymes with artfully modulated multi-enzymatic performances for highly efficient catalytic therapy upon the guidance of multi-modal imaging.

#### *Mn complex-based hollow nanoparticles*

Loading versatile Mn complexes into hollow structures has also become a research topic of high interest. For example, Yan et al. [127] fabricated an all-in-one nanoplatform (denoted as aHNF) with DOX, Ce6 and $Mn^{2+}$ ions co-encapsulated inside the cavity of hollow silica nanoparticles under mild, eco-friendly and convenient reaction conditions, in which partial $Mn^{2+}$ ions were captured by the drug molecules. Finally, the outermost surface was modified with PEG to endow the nanoformulations with good biocompatibility and prolonged blood circulation. In this way, the multiple treatment units could be transported to the tumor tissues and then synergistically functioned to relieve the therapeutic resistance with enhanced antitumor efficacy. Briefly, the nanosystem improved the bioavailability of Ce6 as well as its release behavior, markedly promoting the PDT outcomes. Furthermore, $Mn^{2+}$ not only was able to serve as a good MR imaging CA for diagnosis but also activated a Fenton-like reaction to generate plenty of •OH as well as amplify the DOX- and Ce6-induced cytotoxicity, such as intracellular oxidative stress elevation and oxidation defense disruption. In vivo experiments indicated the unsatisfactory treatment effects of chemotherapy even with the involvement of $Mn^{2+}$, but the combined group displayed significant tumor inhibition after PDT inclusion as revealed by the remarkably decreased tumor volumes. Additionally, the nanoformulations could be completely degraded in the physiological environment and caused no significant side effects in vitro and in vivo.

Manganese carbonyl (MnCO), as a prodrug of CO gas and $Mn^{2+}$possesses bright prospects in cancer theranostics due to the following merits: (1) Gas therapy does not cause drug resistance but is able to sensitize drug-resistant cells to chemotherapeutic drugs. (2) Gas therapy is regarded as a green therapeutic method that induces

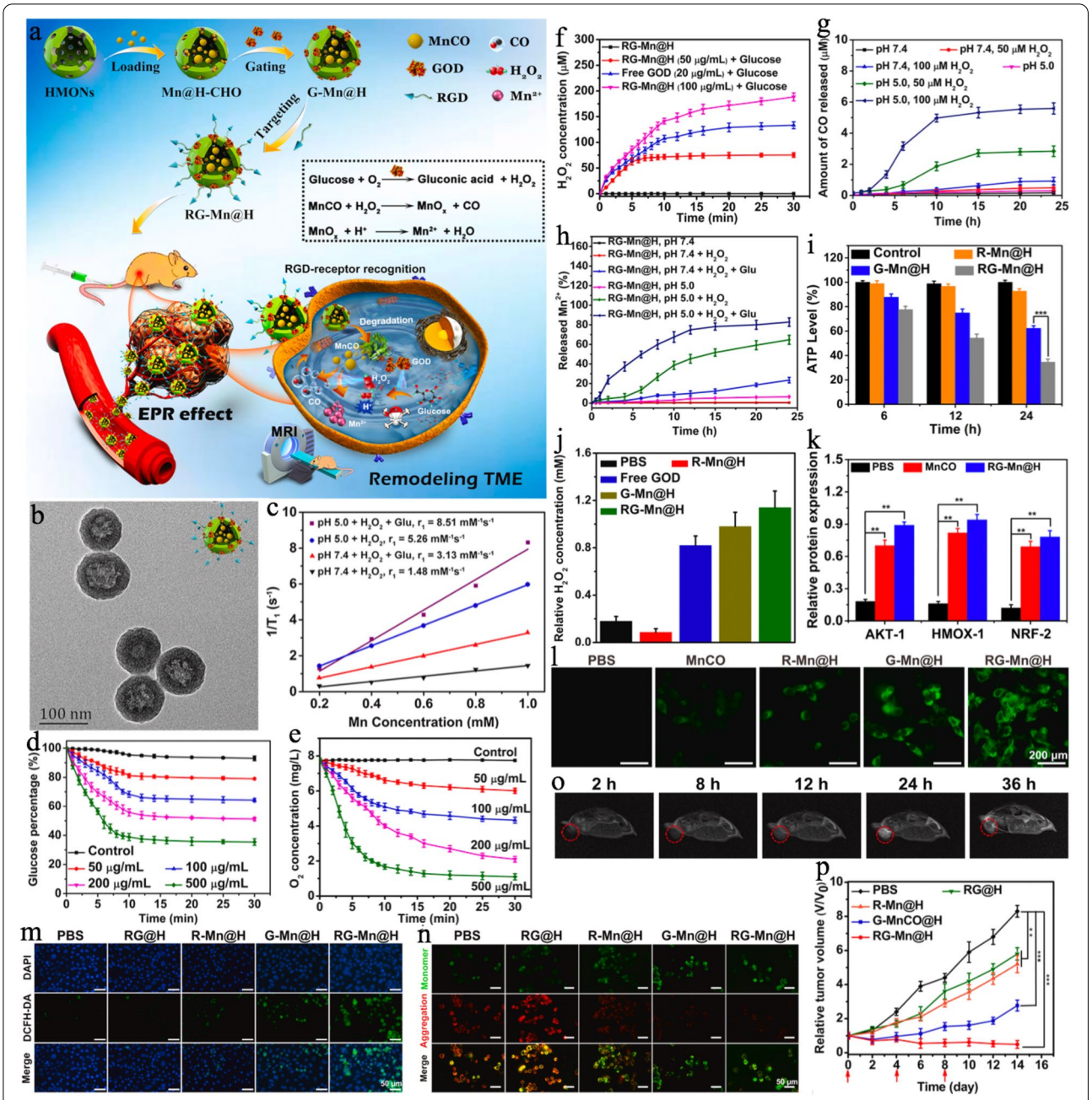


**Fig. 6** **a** Schematic illustrations of the construction of targeted cascade nanocatalyst (RG-Mn@H) for remodeling TME, the sequential cascade reactions mechanism of RG-Mn@H on the generation of $H_2O_2$ for controllable CO release, and MR imaging-monitored combinatorial therapy of breast cancer. **b** TEM image of RG-Mn@H. **c** Relaxivity fits of RG-Mn@H in PBS solutions (50 μM of $H_2O_2$, pH 5.0 or 7.4) with or without addition of glucose. **d** Glucose concentration and (**e**) Oxygen concentration plotted against time in different concentrations of RG-Mn@H solution with the addition of glucose (10 mM) and $H_2O_2$ (50 μM). **f** The change of $H_2O_2$ concentrations in the glucose solution (10 mM) with the addition of RG-Mn@H (50 or 100 μg/mL) and free GOD (20 μg/mL). **g** In vitro cumulative release of CO from RG-Mn@H at different pH values with different amounts of $H_2O_2$. **h** The release profile of $Mn^{2+}$ from RG-Mn@H (3 mg/mL) in PBS solutions (pH 5.0 or 7.4) with or without addition of glucose (Glu) and $H_2O_2$. **i** ATP level in MDA-MB 231 cells after different treatments as indicated. ***$P < 0.001$. Error bars indicate standard deviation ($n = 5$). **j** The $H_2O_2$ level in MDA-MB-231 cells after different treatments ([Mn]: 10 μg/mL). **k** Quantitative results of the Akt-1, Nrf-2, and HMOX-1 expression after different treatments. **$P < 0.01$. Error bars indicate standard deviation ($n = 3$). **l** Intracellular CO level detected by using COP-1 CO fluorescence probe ([Mn]: 10 μg/mL). Fluorescence images of MDA-MB-231 cells after different treatments and stained with (**m**) intracellular DCFH-DA probe and (**n**) JC-1 dye (red, aggregates; green, monomers). **o** In vivo $T_1$-weighted MR images of the tumor bearing mice at different time points after i.v. injection of RG-Mn@H (Mn: 5 mg/kg, tumors are indicated by the red rings). **p** The tumor growth curves during different treatments ($n = 5$). Reproduced with permission from Ref. [129]. Copyright 2021, Elsevier Inc.

no significant systemic toxicity or side effects. (3) The resultant $Mn^{2+}$ can act as both a good MR imaging CA and Fenton-like agent [128]. For example, Wu et al. [129] proposed a "TME remodelling" nanoplatform (RGD-GOD-MnCO@HMONs, denoted RG-Mn@H) for in situ continued CO release and cancer-specific MR imaging-guided synergistic gas/starvation therapy (Fig. 6a). The biodegradable HMON cores were the key to this design, which not only encapsulated MnCO but also enabled glucose oxidase (GOD) to grow on the surface. The pH-sensitive GOD acted as a gatekeeper to avoid the premature leakage of MnCO and facilitated further modification with the tumor-targeting unit RGD. The monodispersed RG-Mn@H displayed a hollow spherical morphology with an average particle size of approximately 100.8 nm, and the catalytic behavior of GOD was evidenced by the decrease of glucose/$O_2$ level and increase of $H_2O_2$ concentration (Fig. 6b and d-f). The elevated acidity resulted in the dissociation of GOD and subsequently caused the release of the loaded MnCO, which was further decomposed to CO and $Mn^{2+}$ ions by the generated $H_2O_2$ (Fig. 6g, h). These features were systematically investigated at the cellular level, and the ATP level was dramatically decreased in the RG-Mn@H group; however, the corresponding $H_2O_2$ concentration was significantly enhanced that could promote the production of CO (Fig. 6i, j and l). Interestingly, the generated CO was able in turn to boost ROS formation, resulting in the intensive green fluorescence of DCF in the RG-Mn@H group (Fig. 6m). Moreover, the R-Mn@H-, G-Mn@H- and RG-Mn@H-treated cells displayed stronger green fluorescence, indicating the efficient induction of mitochondrial dysfunction by CO (Fig. 6n). Furthermore, western blotting analysis showed the significant up-regulation of Akt-1, Nrf-2, and HMOX-1, which demonstrated that the release of CO activated the Akt signalling pathway to amplify the treatment outcome (Fig. 6k). Notably, tumor growth was markedly and synergistically suppressed after RG-Mn@H treatment, resulting in a much higher inhibition rate (94.3%) than R–Mn@H (inhibition rate = 35.5%) or G-Mn@H (inhibition rate = 66.7%) (Fig. 6p). Additionally, the released paramagnetic $Mn^{2+}$ ions could be used for $T_1$-weighted MR imaging ($r_1 = 8.51\ mM^{-1}s^{-1}$ in acidic $H_2O_2$/glucose solution) that monitored the treatment process (Fig. 6c and o). This intelligent nanoreactor holds unique potential for cancer-targeted imaging and augmenting gas-induced therapy.

Analogously, Zheng et al. [130] loaded MnCO into the cavity of hollow mesoporous CuS nanoparticles for MR imaging-guided combined PTT/gas therapy. The multifunctional MnCO@CuS was proven to possess good biocompatibility and low toxicity. Once accumulated in tumor tissues, the overproduced $H_2O_2$ could trigger the release of CO from MnCO, which was further accelerated upon NIR irradiation. Meanwhile, the intermediate $MnO_x$ was decomposed to $Mn^{2+}$ to allow $T_1$-weighted MR imaging ($r_1 = 8.64\ mM^{-1}s^{-1}$ when treated with pH 5.5 + 100 μM $H_2O_2$ + NIR) in the presence of acidic TME. In vitro and in vivo experiments demonstrated that MnCO@CuS + Laser exhibited the strongest anticancer effects; only 3.56% of the cells survived, and tumors in this group were almost completely eradicated at 14 days post-injection.

### Dual-magnetic-cores Mn-based hollow nanoplatforms for MR imaging-guided cancer therapies

In addition to Mn, Co- and Fe-based nanomaterials have attracted tremendous attention in the biomedical field [131–135]. Generally, nanomaterials containing Co and Fe are good $T_2$-weighted MR imaging CAs and Fenton−/Fenton-like agents due to their intrinsic magnetic and catalytic properties, respectively. In addition, they display great potential in magnetic hyperthermia and PTT, which can synergize with other diagnosis and treatment functions [136–139]. In this section, we will present dual magnetic cores, including Mn-Co-based and Mn-Fe-based nanoplatforms, for cancer theranostics.

A size-tunable hollow nanoplatform (manganese/cobalt oxide, denoted as MCO NP) was reported by Ren et al. [140] for $T_1$-$T_2$ dual-modal MR imaging and drug delivery (Fig. 7a). Hollow MCO was synthesized by a one-step redox reaction of PAA-stabilized Co nanoparticles and $KMnO_4$. The hollow cavities were formed due to the Kirkendall effect, i.e., the different diffusion rates of $MnO_4^-$ and Co atoms. By varying the PAA amount, the MCO NP could be synthesized with controlled diameters ranging from 50 to 300 nm. Taking the 70 nm-MCO NP with a cavity size of 30 nm as an example, it proved to be a desirable nanocarrier for hydrophilic DOX loading by diffusion into the cavity and electrostatic interactions with PAA. Subsequent experiments demonstrated that the DOX-encapsulated MCO NP acted as both GSH-triggered CAs and DDSs for tumor diagnosis and chemotherapy. In contrast to the intact MCO, the $T_1$- and $T_2$-weighted MR imaging signals were obviously enhanced after degradation by GSH, reaching a 2.24- and 3.43-fold increment, respectively. At the same time, effective killing effects towards cancer cells and significant tumor suppression were noticed as a result of the released DOX.

Ferric hexacyanoferrate, also known as Prussian blue (PB), is a biocompatible photothermal agent that has been extensively investigated for cancer therapy, but its single therapeutic function with insufficient

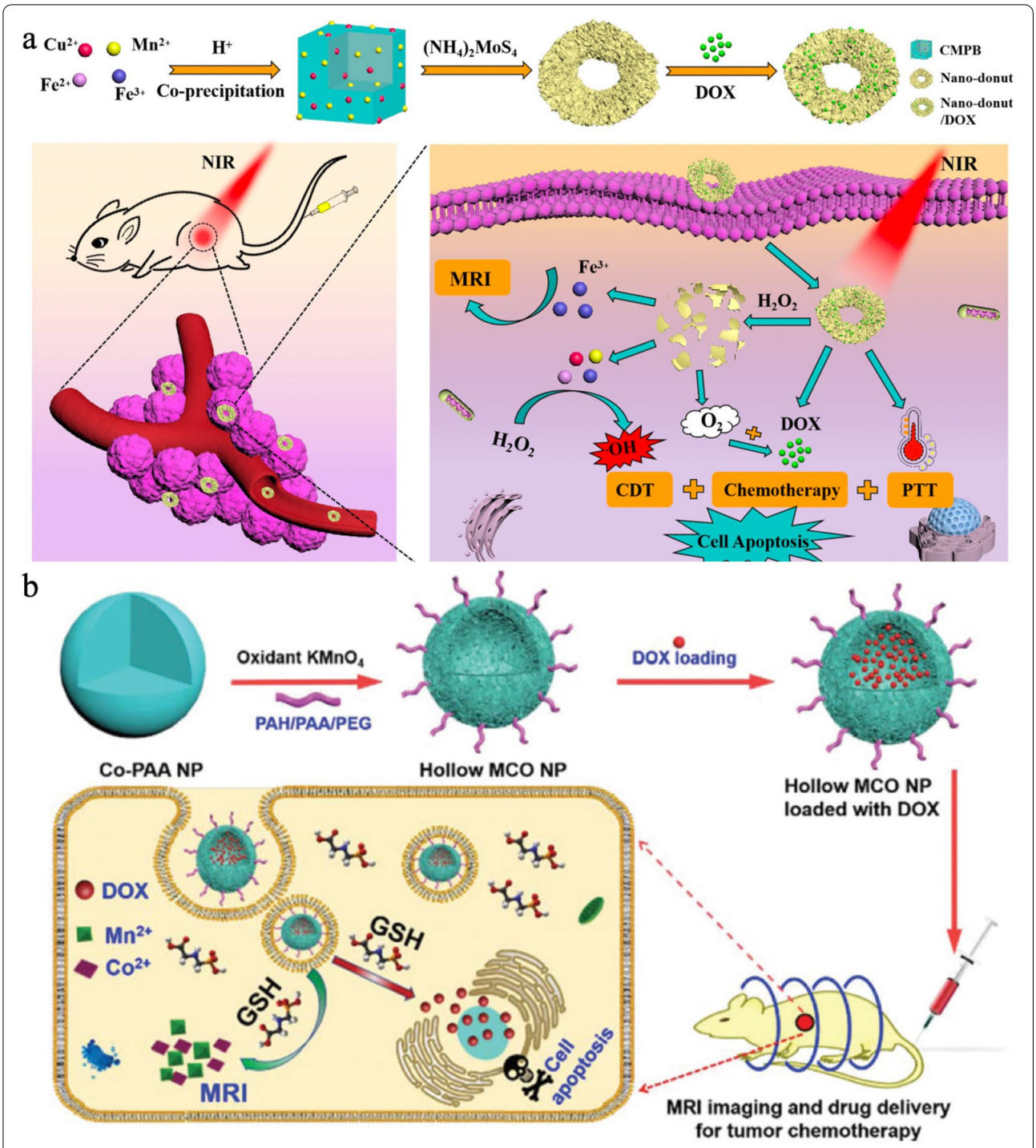


**Fig. 7** **a** Scheme of the synthesis process and therapeutic mechanism of Nano-donut/DOX nanoplatforms. Reproduced with permission from Ref. [141]. Copyright 2022, Elsevier Inc. **b** The schematic illustration of MCO NP synthesis and their application as GSH-responsive nanoscale DDSs. Reproduced with permission from Ref. [140]. Copyright 2019, The Royal Society of Chemistry

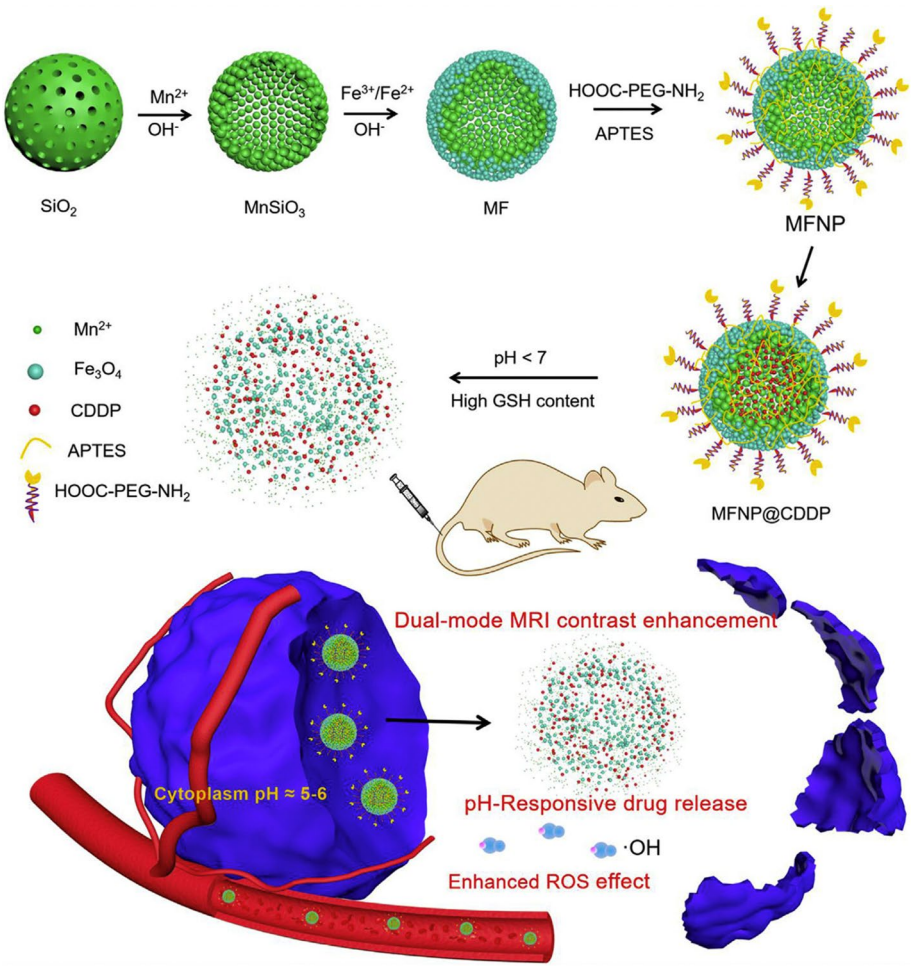


**Fig. 8** Schematic illustration of the synthetic procedure for MFNP and the nanoplatform integrating dual-mode MR imaging, drug delivery, and ROS generation abilities for cancer diagnosis and therapy. Reproduced with permission from Ref. [145]. Copyright 2022, Elsevier Inc.

photothermal effect still hampers further applications in the clinic [142]. Based on $Cu^{2+}$/$Mn^{2+}$ co-doped PB (CMPB) nanoparticles, Guan et al. [141] fabricated a biodegradable nanoplatform with TME-responsive catalysis for MR imaging and enhanced PTT/CDT/chemotherapy (Fig. 7b). Interestingly, the $(NH_4)_2MoS_4$ treatment enabled CMPB to form a hollow structure, and the final Nano-donut (CMPB-$MoS_2$-PEG) was obtained after PEG modification. Subsequently, DOX was encapsulated into the cavity of the Nano-donut and could be delivered to the tumor site to amplify the therapeutic effects. The Nano-donut showed rapid responsiveness to endogenous $H_2O_2$, leading to decomposition of the framework. The released multivalent elements (Cu/Fe/Mn ions) were able to decrease the bandgap and thus synergistically promote Fenton/Fenton-like reactions for enhanced CDT. Moreover, the presence of $Mn^{4+}$ could also facilitate $O_2$ generation by reacting with $H_2O_2$ to alleviate the hypoxic TME, improving the chemotherapeutic efficacy of DOX. Furthermore, the mingling of $MoS_2$ and PB significantly enhanced the photothermal conversion efficiency, ranging from 16.02% (PB only) to 38.0%. Additionally, $Fe^{3+}$ was demonstrated to be a decent $T_2$-weighted MR imaging CA to guide the treatment process. In vitro and in vivo experiments clearly revealed the remarkable suppressive effects of Nano-donut/DOX on cancer cells and tumors as well as the excellent biological safety.

Due to the high specific surface area, manganese silicate ($MnSiO_3$) can rapidly respond to the weakly acidic and GSH-overproduced TME, acting as a potent $T_1$-weighted MR imaging CA and benefiting for drug delivery [143, 144]. In order to improve the diagnostic and therapeutic effects, Sun et al. [145] constructed biodegradable $MnSiO_3$@$Fe_3O_4$ (MF) functionalized with PEG (MFNP) and subsequently encapsulated cisplatin (CDDP) to

obtain MFNP@CDDP for $T_1$-$T_2$ dual-modal MR imaging and cooperative cancer treatment (Fig. 8). The decoration of $Fe_3O_4$ nanoparticles on the $MnSiO_3$ surface was capable of effectively obstructing the pores of $MnSiO_3$ and reducing the premature leakage of loaded CDDP. When the TME was reached, the inner $MnSiO_3$ quickly reacted with the weak acid and overproduced GSH, resulting in the collapse of MFNP@CDDP, i.e., the $Fe_3O_4$ nanoparticles separated and CDDP/$Mn^{2+}$ were rapidly released. The resultant $Fe_3O_4$ and $Mn^{2+}$ helped decrease the interference between their $T_1$ and $T_2$ contrast capabilities, enhancing the dual-modal MR imaging performance ($r_1 = 12.24\,mM^{-1}s^{-1}$ and $r_2 = 66.62\,mM^{-1}s^{-1}$ at pH 5.5, GSH 10 mM). Additionally, the Fenton-like reaction of $Fe_3O_4$ was boosted during the exfoliation process owing to the increased specific surface area; thus, more highly toxic •OH was generated to induce HeLa cell apoptosis. The therapeutic effects followed the order MFNP@CDDP > CDDP > MFNP, demonstrating the excellent antitumor efficacy of MFNP@CDDP, which was superior to that of CDT or chemotherapy alone.

## Conclusion and perspectives

Over the past decade, the utilization of Mn-based nanoplatforms, especially Mn-based hollow nanoplatforms, has shown promising prospects in cancer theranostics. In this work, we systematically describe the recent advances in Mn-based hollow nanoplatforms, including $Mn_xO_y$, hollow matrix-supported $Mn_xO_y$, Mn-doped hollow nanoparticles, Mn complex-based hollow nanoparticles, hollow Mn-Co nanoparticles and hollow Mn-Fe nanoparticles, for MR imaging-guided therapies. In addition to intrinsic MR imaging and CDT, such hollow nanosystems are also expected to realize synergistic diagnostic and therapeutic effects by rational design and optimization, in which FL imaging, PA imaging, CT imaging, chemotherapy, RT, PTT, PDT, ST and gas therapy can be integrated to compensate for the inadequacies of single-modal diagnosis and treatment. For better comparison, we have summarized the above-mentioned hollow nanoplatforms in terms of materials, templates and mechanisms as well as biomedical applications (Table 1). In short, the encouraging progress in biomedicine presented here brings us much closer to an exciting new paradigm for cancer theranostics. In consideration of the current hurdles and challenges in exploring Mn-based hollow nanoplatforms for clinical applications, our perspectives are as follows:

(1) Safety is one of the most important concerns for clinically translational nanomedicine. Desirable nanotheranostics should exhibit non-toxicity at normal physiological environments but recover their imaging features and generate a large number of therapeutic species for various treatments. Although $MnO_2$ has been proven to possess low toxicity and good biocompatibility biodegradability, the introduced substances and hollow matrix may raise the risk of toxicity. More detailed biological and biosafety assessments of these Mn-based hollow nanoplatforms are in urgent need, and their potential risks should be further evaluated, adding chronic toxicity evaluation to the current acute toxicity assessments. In addition, the biodistribution, excretion and potential harm towards specific organs also need to be explored. At present, most in vivo experiments are carried out on mice, and large animal models such

**Table 1** Summary of various hollow nanoplatforms for cancer theranostics

| Materials | Templates and mechanisms | Biomedical applications | References |
|---|---|---|---|
| PLTM-HM$nO_2$@Bu | PLGA | $T_1$-weighted MR imaging and CDT/chemotherapy | [81] |
| H-M$nO_2$/DOX/BPQDs | $SiO_2$ | $T_1$-weighted MR/FL imaging and chemotherapy/PDT/PTT | [93] |
| CMC | $SiO_2$ | $T_1$-weighted MR imaging and chemotherapy/RT | [97] |
| DOX@HPMO | nanoscale Kirkendall effect | $T_1$-weighted MR imaging and chemotherapy | [98] |
| HPMRCD | $SiO_2$ | $T_1$-weighted MR/FL imaging and chemotherapy/PDT | [71] |
| AAM-Ce6 | galvanic replacement reaction | $T_1$-weighted MR/PA//FL imaging and PTT/PDT | [113] |
| ICG@Mn/Cu/Zn-MOF@$MnO_2$ | Ostwald ripening process | $T_1$-weighted MR/FL/PT imaging and PTT/PDT/CDT | [92] |
| CMH | $SiO_2$ | $T_1$-weighted MR imaging and PDT | [117] |
| DOX-Mn-ZGOCS-PEG | $SiO_2$ | $T_1$-weighted MR/NIR-PL and chemotherapy | [125] |
| PHMZCO-AT | nanoscale Kirkendall effect | $T_1$-weighted MR/CT imaging and CDT | [126] |
| aHNF | calcium carbonate | $T_1$-weighted MR imaging and chemotherapy/PDT | [127] |
| RG-Mn@H | $SiO_2$ | $T_1$-weighted MR imaging and ST/gas therapy | [129] |
| MnCO@CuS | Ostwald ripening process | $T_1$-weighted MR imaging and PTT/gas therapy | [130] |
| CMPB-M$oS_2$-PEG | Ostwald ripening process | $T_2$-weighted MR imaging and PTT/CDT/chemotherapy | [141] |
| MFNP@CDDP | $SiO_2$ | $T_1$−/$T_2$-weighted MR imaging and CDT/chemotherapy | [145] |
| DOX-encapsulated MCO | nanoscale Kirkendall effect | $T_1$−/$T_2$-weighted MR imaging and chemotherapy | [140] |

primates, should be updated to better investigate the toxicities in the body.

(2) Cancer-specific units, including platelets, cancer cell membranes and RGD have been adopted in these Mn-based hollow nanoplatforms, but the majority of them are decorated with PEG and other polymers, such as polyvinyl pyrrolidone (PVP) or ZDS, to improve the physiological stability, biocompatibility and blood circulation time. Further studies should focus on the development of active targeting nanoplatforms, aiming to facilitate considerable tumor accumulation and promoting diagnostic and therapeutic effects. Notably, the fabrication of organelle-targeted nanoplatforms has been regarded as one of the hottest topics in recent years [146–149]. Triphenyl phosphonium (TPP), a typical mitochondrial targeting molecule, favours ROS/gas-mediated therapies [150–152]. For instance, a multifunctional nanotheranostic based on TPP-modified hollow CuS was reported to integrate hypoxia-activated chemotherapy, PDT and PTT for synergistically treating cancer and maximizing the therapeutic biowindow [153]. Other organelles, such as the nucleus and lysosome, are also good targets for constructing highly effective cancer-specific theranostics [154, 155].

(3) Notably, multi-modal treatment modalities could significantly enhance curative outcomes, and more efforts should be made to explore synergistic manners rather than simply combining them. For instance, PTT has been demonstrated to increase the oxygen flow and the catalytic reaction rates, which is beneficial for PDT, CDT, etc. In light of these, the photothermal agents that are incorporated into the hollow structures should be equipped with desired PCE and photostability. In addition, the laser wavelength used for PTT should be extended to the NIR-II region and even farther away.

(4) The size of the hollow nanoplatforms and the cavity volume should be adjusted to increase tumor accumulation and drug-loading efficiency, respectively. In addition, a facile and mild synthetic strategy for mass production of hollow nanoplatforms is of great significance before clinical applications. Compared to the sacrificial template-based method, the self-templating method seems to be more appealing as a result of the simple preparation process and reduced chemical waste formation.

Although many issues remain unresolved, we believe that Mn-based hollow nanoplatforms will reach their full potential for translation from bench to bedside with future advances in materials science, chemistry, physics, and medicine.

**Acknowledgements**
Not applicable.

**Authors' contributions**
LZ, WZ and GL developed the idea and structure of the review article. SL and LZ compiled, analyzed all relevant documents and wrote the manuscript. WZ and GL edited and finalized the manuscript and provided funding supports. All authors read and approved the final manuscript.

**Funding**
The work was supported by Key Program of the National Natural Science Foundation of China (Grant No. 81730049) and Startup Funding for Scientific Research of China University of Geosciences (Wuhan).

**Availability of data and materials**
Data sharing is not applicable to this article as no datasets were generated or analysed during the current study.

## Declarations

**Ethics approval and consent to participate**
Not applicable.

**Consent for publication**
Not applicable.

**Competing interests**
The authors declare that they have no competing interests.

Received: 14 April 2022 Accepted: 10 June 2022
Published online: 06 July 2022

**References**

1. Liao G, He F, Li Q, Zhong L, Zhao R, Che H, et al. Emerging graphitic carbon nitride-based materials for biomedical applications. Prog Mater Sci. 2020;112:100666.
2. Zhang L, Fan Y, Yang Z, Yang M, Wong C-Y. NIR-II-driven and glutathione depletion-enhanced hypoxia-irrelevant free radical nanogenerator for combined cancer therapy. J Nanobiotechnol. 2021;19(1):1–16.
3. Mo Z, Qiu M, Zhao K, Hu H, Xu Q, Cao J, et al. Multifunctional phototheranostic nanoplatform based on polydopamine-manganese dioxide-IR780 iodide for effective magnetic resonance imaging-guided synergistic photodynamic/photothermal therapy. J Colloid Interface Sci. 2022;611:193–204.
4. Zou Y, Jin H, Sun F, Dai X, Xu Z, Yang S, et al. Design and synthesis of a Lead sulfide based Nanotheranostic agent for computer tomography/magnetic resonance dual-mode-bioimaging-guided Photothermal therapy. ACS Appl Nano Mater. 2018;1:2294–305.
5. Zhang L, Forgham H, Huang X, Shen A, Davis T, Qiao R, et al. All-in-one inorganic nanoagents for near-infrared-II photothermal-based cancer theranostics. Mater Today Adv. 2022;14:100226.
6. Qin Z, Qiu M, Zhang Q, Yang S, Liao G, Xiong Z, et al. Development of copper vacancy defects in a silver-doped CuS nanoplatform for high-efficiency photothermal–chemodynamic synergistic antitumor therapy. J Mater Chem B. 2021;9:8882–96.
7. Zhang P, Li Y, Tang W, Zhao J, Jing L, McHugh KJ. Theranostic nanoparticles with disease-specific administration strategies. Nano Today. 2022;42:101335.
8. Tao Q, He G, Ye S, Zhang D, Zhang Z, Qi L, et al. Mn doped Prussian blue nanoparticles for $T_1/T_2$ MR imaging, PA imaging and Fenton reaction enhanced mild temperature photothermal therapy of tumor. J Nanobiotechnol. 2022;20(1):1–14.
9. Zou Y, Sun F, Liu C, Yu C, Zhang M, He Q, et al. A novel nanotheranostic agent for dual-mode imaging-guided cancer therapy based on europium complexes-grafted-oxidative dopamine. Chem Eng J. 2019;357:237–47.
10. Zhang M, Zou Y, Zhong Y, Liao G, Yu C, Xu Z. Polydopamine-based tumor-targeted multifunctional reagents for computer tomography/fluorescence dual-mode bioimaging-guided Photothermal therapy. ACS Appl Bio Mater. 2019;2:630–7.
11. Jiao W, Zhang T, Peng M, Yi J, He Y, Fan H. Design of Magnetic Nanoplatforms for Cancer Theranostics. Biosensors. 2022;12(1):38.
12. Chen C, Ge J, Gao Y, Chen L, Cui J, Zeng J, et al. Ultrasmall superparamagnetic iron oxide nanoparticles: A next generation contrast

agent for magnetic resonance imaging. Wires Nanomed Nanobi. 2022;14(1):e1740.
13. Zhang L, Liu R, Peng H, Li P, Xu Z, Whittaker AK. The evolution of gadolinium based contrast agents: from single-modality to multi-modality. Nanoscale. 2016;8(20):10491–510.
14. Clough TJ, Jiang L, Wong K-L, Long NJ. Ligand design strategies to increase stability of gadolinium-based magnetic resonance imaging contrast agents. Nat Commun. 2019;10(1):1–14.
15. Zhang W, Liu L, Chen H, Hu K, Delahunty I, Gao S, et al. Surface impact on nanoparticle-based magnetic resonance imaging contrast agents. Theranostics. 2018;8(9):2521.
16. Bao Y, Sherwood J, Sun Z. Magnetic iron oxide nanoparticles as $T_1$ contrast agents for magnetic resonance imaging. J Mater Chem C. 2018;6(6):1280–90.
17. Wahsner J, Gale EM, Rodríguez-Rodríguez A, Caravan P. Chemistry of MRI contrast agents: current challenges and new frontiers. Chem Rev. 2018;119(2):957–1057.
18. Na HB, Song IC, Hyeon T. Inorganic nanoparticles for MRI contrast agents. Adv Mater. 2009;21(21):2133–48.
19. Zhang L, Liu Y, Zhang Q, Li T, Yang M, Yao Q, et al. Gadolinium-labeled aminoglycoside and its potential application as a bacteria-targeting magnetic resonance imaging contrast agent. Anal Chem. 2018;90(3):1934–40.
20. Li H, Yang S, Hui D, Hong R. Progress in magnetic $Fe_3O_4$ nanomaterials in magnetic resonance imaging. Nanotechnol Rev. 2020;9(1):1265–83.
21. Little RA, Jamin Y, Boult JK, Naish JH, Watson Y, Cheung S, et al. Mapping hypoxia in renal carcinoma with oxygen-enhanced MRI: comparison with intrinsic susceptibility MRI and pathology. Radiology. 2018;288(3):739–47.
22. Jung H, Park B, Lee C, Cho J, Suh J, Park J, et al. Dual MRI $T_1$ and $T_2^{(*)}$ contrast with size-controlled iron oxide nanoparticles. Nanomed Nanotechnol Biol Med. 2014;10(8):1679–89.
23. Lee SH, Kim BH, Na HB, Hyeon T. Paramagnetic inorganic nanoparticles as $T_1$ MRI contrast agents. Wires Nanomed Nanobi. 2014;6(2):196–209.
24. Zhao W, Yu X, Peng S, Luo Y, Li J, Lu L. Construction of nanomaterials as contrast agents or probes for glioma imaging. J Nanobiotechnol. 2021;19(1):1–31.
25. Shiraishi K, Kawano K, Maitani Y, Yokoyama M. Polyion complex micelle MRI contrast agents from poly (ethylene glycol)-b-poly (L-lysine) block copolymers having Gd-DOTA; preparations and their control of $T_1$-relaxivities and blood circulation characteristics. J Control Release. 2010;148(2):160–7.
26. Anani T, Rahmati S, Nayer Sultana AED. MRI-traceable theranostic nanoparticles for targeted cancer treatment. Theranostics. 2021;11(2):579.
27. Ruan S, Zhou Y, Jiang X, Gao H. Rethinking CRITID procedure of brain targeting drug delivery: circulation, blood brain barrier recognition, intracellular transport, diseased cell targeting, internalization, and drug release. Adv Sci. 2021;8(9):2004025.
28. Ruan J, Qian H. Recent development on controlled synthesis of Mn-based nanostructures for bioimaging and Cancer therapy. Adv Ther. 2021;4(5):2100018.
29. Qian X, Han X, Yu L, Xu T, Chen Y. Manganese-based functional nanoplatforms: Nanosynthetic construction, physiochemical property, and theranostic applicability. Adv Funct Mater. 2020;30(3):1907066.
30. García-Hevia L, Bañobre-López M, Gallo J. Recent Progress on manganese-based nanostructures as responsive MRI contrast agents. Chem-Eur J. 2019;25(2):431–41.
31. Haque S, Tripathy S, Patra C. Manganese based advanced nanoparticles for biomedical applications: future opportunity and challenges. Nanoscale. 2021;13:16405–26.
32. He T, Qin X, Jiang C, Jiang D, Lei S, Lin J, et al. Tumor pH-responsive metastable-phase manganese sulfide nanotheranostics for traceable hydrogen sulfide gas therapy primed chemodynamic therapy. Theranostics. 2020;10(6):2453.
33. Yang G, Ji J, Liu Z. Multifunctional $MnO_2$ nanoparticles for tumor microenvironment modulation and cancer therapy. Wires Nanomed Nanobi. 2021;13(6):e1720.
34. Wen J, Yang K, Sun S. $MnO_2$-based nanosystems for cancer therapy. Chem Commun. 2020;56(52):7065–79.
35. Yu L, Chen Y, Wu M, Cai X, Yao H, Zhang L, et al. "Manganese extraction" strategy enables tumor-sensitive biodegradability and theranostics of nanoparticles. J Am Chem Soc. 2016;138(31):9881–94.
36. Jing L, Liang X, Li X, Lin L, Yang Y, Yue X, et al. Mn-porphyrin conjugated au nanoshells encapsulating doxorubicin for potential magnetic resonance imaging and light triggered synergistic therapy of cancer. Theranostics. 2014;4(9):858.
37. Lin X, Fang Y, Tao Z, Gao X, Wang T, Zhao M, et al. Tumor-microenvironment-induced all-in-one nanoplatform for multimodal imaging-guided chemical and photothermal therapy of cancer. ACS Appl Mater Inter. 2019;11(28):25043–53.
38. Zhao N, Yan L, Xue J, Zhang K, Xu F-J. Degradable one-dimensional dextran-iron oxide nanohybrids for MRI-guided synergistic gene/photothermal/magnetolytic therapy. Nano Today. 2021;38:101118.
39. Yuan Y, Zhou R, Li T, Qu S, Bai H, Liang J, et al. Enriched au nanoclusters with mesoporous silica nanoparticles for improved fluorescence/computed tomography dual-modal imaging. Cell Proliferat. 2021;54(4):e13008.
40. Tang T, Chang B, Zhang M, Sun T. Nanoprobe-mediated precise imaging and therapy of glioma. Nanoscale Horiz. 2021;6(8):634–50.
41. Xue D, Liu Y, Jin L, Wang Y, Cui F, Liu J, et al. Novel multifunctional theranostic nanoagents based on $Ho^{3+}$ for CT/MRI dual-modality imaging-guided photothermal therapy. Sci China Chem. 2021;64(4):558–64.
42. Li F, Zhi D, Luo Y, Zhang J, Nan X, Zhang Y, et al. Core/shell $Fe_3O_4$/$Gd_2O_3$ nanocubes as $T_1$–$T_2$ dual modal MRI contrast agents. Nanoscale. 2016;8(25):12826–33.
43. Peng Y-K, Lui CN, Chen Y-W, Chou S-W, Raine E, Chou P-T, et al. Engineering of single magnetic particle carrier for living brain cell imaging: a tunable $T_1$—/$T_2$—/dual-modal contrast agent for magnetic resonance imaging application. Chem Mater. 2017;29(10):4411–7.
44. Zhang L, Liang S, Liu R, Yuan T, Zhang S, Xu Z, et al. Facile preparation of multifunctional uniform magnetic microspheres for $T_1$-$T_2$ dual modal magnetic resonance and optical imaging. Colloids Surf B Biointerfaces. 2016;144:344–54.
45. Wang L, Lin H, Chi X, Sun C, Huang J, Tang X, et al. A self-assembled biocompatible nanoplatform for multimodal MR/fluorescence imaging assisted photothermal therapy and prognosis analysis. Small. 2018;14(35):1801612.
46. Yang R, Hou M, Gao Y, Lu S, Zhang L, Xu Z, et al. Biomineralization-inspired crystallization of manganese oxide on silk fibroin nanoparticles for *in vivo* MR/fluorescence imaging-assisted tri-modal therapy of cancer. Theranostics. 2019;9(21):6314.
47. Hu X, Chen Z, Jin AJ, Yang Z, Gan D, Wu A, et al. Rational Design of all-Organic Nanoplatform for highly efficient MR/NIR-II imaging-guided Cancer Phototheranostics. Small. 2021;17(12):2007566.
48. Du Y, Liu D, Sun M, Shu G, Qi J, You Y, et al. Multifunctional Gd-CuS loaded UCST polymeric micelles for MR/PA imaging-guided chemo-photothermal tumor treatment. Nano Res. 2022;15(3):2288–99.
49. Zhang R, Zeng Q, Li X, Xing D, Zhang T. Versatile gadolinium (III)-phthalocyaninate photoagent for MR/PA imaging-guided parallel photocavitation and photodynamic oxidation at single-laser irradiation. Biomaterials. 2021;275:120993.
50. Tian W, Su Y, Tian Y, Wang S, Su X, Liu Y, et al. Periodic mesoporous Organosilica coated Prussian blue for MR/PA dual-modal imaging-guided Photothermal-chemotherapy of triple negative breast Cancer. Adv Sci. 2017;4(3):1600356.
51. Alvarez-Lorenzo C, Concheiro A. Smart drug delivery systems: from fundamentals to the clinic. Chem Commun. 2014;50(58):7743–65.
52. Wang S, Liu H, Wu D, Wang X. Temperature and pH dual-stimuli-responsive phase-change microcapsules for multipurpose applications in smart drug delivery. J Colloid Interface Sci. 2021;583:470–86.
53. Tian B, Liu Y, Liu J. Smart stimuli-responsive drug delivery systems based on cyclodextrin: a review. Carbohydr Polym. 2021;251:116871.
54. Mohan T, Ajdnik U, Nagaraj C, Lackner F, Dobaj Štiglic A, Palani T, et al. One-step fabrication of hollow spherical cellulose beads: application in pH-responsive therapeutic delivery. ACS Appl Mater Inter. 2022;14(3):3726–39.
55. Zhao D, Yang N, Xu L, Du J, Yang Y, Wang D. Hollow structures as drug carriers: recognition, response, and release. Nano Res. 2022;15(2):739–57.

56. Yan K, Mu C, Zhang C, Xu Q, Xu Z, Wang D, et al. Pt nanoenzyme decorated yolk-shell nanoplatform as an oxygen generator for enhanced multi-modality imaging-guided phototherapy. J Colloid Interface Sci. 2022;616:759–68.
57. Deng Z, Zhen Z, Hu X, Wu S, Xu Z, Chu PK. Hollow chitosan–silica nanospheres as pH-sensitive targeted delivery carriers in breast cancer therapy. Biomaterials. 2011;32(21):4976–86.
58. Wu F, Zhang M, Lu H, Liang D, Huang Y, Xia Y, et al. Triple stimuli-responsive magnetic hollow porous carbon-based nanodrug delivery system for magnetic resonance imaging-guided synergistic photothermal/chemotherapy of cancer. ACS Appl Mater Inter. 2018;10(26):21939–49.
59. Pan X, Wang W, Huang Z, Liu S, Guo J, Zhang F, et al. MOF-derived double-layer hollow nanoparticles with oxygen generation ability for multimodal imaging-guided Sonodynamic therapy. Angew Chem Int Edit. 2022;132(32):13659–63.
60. Sun X, He G, Xiong C, Wang C, Lian X, Hu L, et al. One-pot fabrication of hollow porphyrinic MOF nanoparticles with ultrahigh drug loading toward controlled delivery and synergistic cancer therapy. ACS Appl Mater Inter. 2021;13(3):3679–93.
61. Guo W, Chen Z, Chen J, Feng X, Yang Y, Huang H, et al. Biodegradable hollow mesoporous organosilica nanotheranostics (HMON) for multimode imaging and mild photo-therapeutic-induced mitochondrial damage on gastric cancer. J Nanobiotechnol. 2020;18(1):1–18.
62. Lin K, Gan Y, Zhu P, Li S, Lin C, Yu S, et al. Hollow mesoporous polydopamine nanospheres: synthesis, biocompatibility and drug delivery. Nanotechnology. 2021;32(28):285602.
63. Wang J, Liu L, You Q, Song Y, Sun Q, Wang Y, et al. All-in-one theranostic nanoplatform based on hollow $MoS_x$ for photothermally-maneuvered oxygen self-enriched photodynamic therapy. Theranostics. 2018;8(4):955.
64. Zhu M, Cheng Y, Luo Q, El-khateeb M, Zhang Q. A review of synthetic approaches to hollow nanostructures. Mater Chem Front. 2021;5(6):2552–87.
65. Fang X, Zhao X, Fang W, Chen C, Zheng N. Self-templating synthesis of hollow mesoporous silica and their applications in catalysis and drug delivery. Nanoscale. 2013;5(6):2205–18.
66. Lin LS, Song J, Yang HH, Chen X. Yolk–Shell nanostructures: design, synthesis, and biomedical applications. Adv Mater. 2018;30(6):1704639.
67. Wang J, Li N. Functional hollow nanostructures for imaging and phototherapy of tumors. J Mater Chem B. 2017;5(43):8430–45.
68. Xu W, Qing X, Liu S, Yang D, Dong X, Zhang Y. Hollow Mesoporous Manganese Oxides: Application in Cancer Diagnosis and Therapy. Small. 2022;18(15):e2106511.
69. Xu X, Duan J, Liu Y, Kuang Y, Duan J, Liao T, et al. Multi-stimuli responsive hollow $MnO_2$-based drug delivery system for magnetic resonance imaging and combined chemo-chemodynamic cancer therapy. Acta Biomater. 2021;126:445–62.
70. Yang G, Xu L, Chao Y, Xu J, Sun X, Wu Y, et al. Hollow $MnO_2$ as a tumor-microenvironment-responsive biodegradable nano-platform for combination therapy favoring antitumor immune responses. Nat Commun. 2017;8(1):1–13.
71. Wang H, Wang W, Liu L, Wang M, Li G, Li H, et al. Biodegradable hollow Polydopamine@manganese dioxide as an oxygen self-supplied Nanoplatform for boosting chemo-photodynamic Cancer therapy. ACS Appl Mater Inter. 2021;13(48):57009–22.
72. Tan L, Tang W, Liu T, Ren X, Fu C, Liu B, et al. Biocompatible hollow polydopamine nanoparticles loaded ionic liquid enhanced tumor microwave thermal ablation *in vivo*. ACS Appl Mater Inter. 2016;8(18):11237–45.
73. Liu C, Chen Z, Wang Z, Li W, Ju E, Yan Z, et al. A graphitic hollow carbon nitride nanosphere as a novel photochemical internalization agent for targeted and stimuli-responsive cancer therapy. Nanoscale. 2016;8(25):12570–8.
74. Zhang L, Wang P, Zheng W, Jiang X. Hollow carbon nanospheres for targeted delivery of chemotherapeutics in breast cancer therapy. J Mater Chem B. 2017;5(32):6601–7.
75. Huang L, Feng J, Fan W, Tang W, Rong X, Liao W, et al. Intelligent pore switch of hollow mesoporous Organosilica nanoparticles for high contrast magnetic resonance imaging and tumor-specific chemotherapy. Nano Lett. 2021;21(22):9551–9.
76. Lu N, Fan W, Yi X, Wang S, Wang Z, Tian R, et al. Biodegradable hollow mesoporous organosilica nanotheranostics for mild hyperthermia-induced bubble-enhanced oxygen-sensitized radiotherapy. ACS Nano. 2018;12(2):1580–91.
77. Wei R, Xu Y, Xue M. Hollow iron oxide nanomaterials: synthesis, functionalization, and biomedical applications. J Mater Chem B. 2021;9(8):1965–79.
78. Song G, Han L, Zou W, Xiao Z, Huang X, Qin Z, et al. A novel photothermal nanocrystals of $Cu_7S_4$ hollow structure for efficient ablation of cancer cells. Nano Micro Lett. 2014;6(2):169–77.
79. Jiang T, Song J, Zhang W, Wang H, Li X, Xia R, et al. Au–ag@au hollow nanostructure with enhanced chemical stability and improved photothermal transduction efficiency for cancer treatment. ACS Appl Mater Inter. 2015;7(39):21985–94.
80. Meng X, Zhou K, Qian Y, Liu H, Wang X, Lin Y, et al. Hollow cuprous oxide@nitrogen-doped carbon Nanocapsules for Cascade Chemodynamic therapy. Small. 2022;18(15):e2107422.
81. Wang H, Bremner DH, Wu K, Gong X, Fan Q, Xie X, et al. Platelet membrane biomimetic bufalin-loaded hollow $MnO_2$ nanoparticles for MRI-guided chemo-chemodynamic combined therapy of cancer. Chem Eng J. 2020;382:122848.
82. Huang J, Huang Y, Xue Z, Zeng S. Tumor microenvironment responsive hollow mesoporous $Co_9S_8$@$MnO_2$-ICG/DOX intelligent nanoplatform for synergistically enhanced tumor multimodal therapy. Biomaterials. 2020;262:120346.
83. Bi H, Dai Y, Yang P, Xu J, Yang D, Gai S, et al. Glutathione and $H_2O_2$ consumption promoted photodynamic and chemotherapy based on biodegradable $MnO_2$–Pt@$Au_{25}$ nanosheets. Chem Eng J. 2019;356:543–53.
84. Cong C, He Y, Zhao S, Zhang X, Li L, Wang D, et al. Diagnostic and therapeutic nanoenzymes for enhanced chemotherapy and photodynamic therapy. J Mater Chem B. 2021;9(18):3925–34.
85. Yi X, Chen L, Zhong X, Gao R, Qian Y, Wu F, et al. Core–shell au@$MnO_2$ nanoparticles for enhanced radiotherapy via improving the tumor oxygenation. Nano Res. 2016;9(11):3267–78.
86. Wang L, Niu M, Zheng C, Zhao H, Niu X, Li L, et al. A core–shell nanoplatform for synergistic enhanced sonodynamic therapy of hypoxic tumor via cascaded strategy. Adv Healthc Mater. 2018;7(22):1800819.
87. Zhang L, Yang Z, He W, Ren J, Wong C-Y. One-pot synthesis of a self-reinforcing cascade bioreactor for combined photodynamic/chemodynamic/starvation therapy. J Colloid Interface Sci. 2021;599:543–55.
88. Xiong Y, Xiao C, Li Z, Yang X. Engineering nanomedicine for glutathione depletion-augmented cancer therapy. Chem Soc Rev. 2021;50(10):6013–41.
89. Lin LS, Song J, Song L, Ke K, Liu Y, Zhou Z, et al. Simultaneous Fenton-like ion delivery and glutathione depletion by $MnO_2$-based nanoagent to enhance chemodynamic therapy. Angew Chem Int Edit. 2018;130(18):4996–5000.
90. Yao Y, Li N, Zhang X, Ong'achwa Machuki J, Yang D, Yu Y, et al. DNA-templated silver nanocluster/porphyrin/$MnO_2$ platform for label-free intracellular $Zn^{2+}$ imaging and fluorescence—/magnetic resonance imaging-guided photodynamic therapy. ACS Appl Mater Inter. 2019;11(15):13991–4003.
91. Cheng M, Yu Y, Huang W, Fang M, Chen Y, Wang C, et al. Monodisperse hollow $MnO_2$ with biodegradability for efficient targeted drug delivery. ACS Biomater Sci Eng. 2020;6(9):4985–92.
92. Cheng Y, Wen C, Sun YQ, Yu H, Yin XB. Mixed-metal MOF-derived hollow porous nanocomposite for Trimodality imaging guided reactive oxygen species-augmented synergistic therapy. Adv Funct Mater. 2021;31(37):2104378.
93. Wu Y, Chen Z, Yao Z, Zhao K, Shao F, Su J, et al. Black phosphorus quantum dots encapsulated biodegradable hollow mesoporous $MnO_2$: dual-modality Cancer imaging and synergistic chemo-phototherapy. Adv Funct Mater. 2021;31(41):2104643.
94. Kukreja A, Kang B, Han S, Shin M-K, Son HY, Choi Y, et al. Inner structure- and surface-controlled hollow MnO nanocubes for high sensitive MR imaging contrast effect. Nano Converg. 2020;7(1):1–11.
95. Lee J, Kumari N, Kim SM, Kim S, Jeon K-W, Im GH, et al. Anchoring ligand-effect on bright contrast-enhancing property of hollow $Mn_3O_4$ nanoparticle in $T_1$-weighted magnetic resonance imaging. Chem Mater. 2018;30(12):4056–64.

96. Sun J, Xu L, Shi Z, Zhao Q, Wang H, Gan T. Morphology-tunable hollow $Mn_2O_3$ nanostructures: highly efficient electrocatalysts and their electrochemical sensing for phenolic endocrine disruptors via toughening of graphene oxide. Sensors Actuators B Chem. 2021;327:128889.
97. Zhu D, Lyu M, Jiang W, Suo M, Huang Q, Li K. A biomimetic nanozyme/camptothecin hybrid system for synergistically enhanced radiotherapy. J Mater Chem B. 2020;8(24):5312–9.
98. Wei R, Gong X, Lin H, Zhang K, Li A, Liu K, et al. Versatile octapod-shaped hollow porous manganese(II) oxide nanoplatform for real-time visualization of cargo delivery. Nano Lett. 2019;19(8):5394–402.
99. Fang J, Wang Q, Yang G, Xiao X, Li L, Yu T. Albumin-$MnO_2$ gated hollow mesoporous silica nanosystem for modulating tumor hypoxia and synergetic therapy of cervical carcinoma. Colloids Surf B Biointerfaces. 2019;179:250–9.
100. Dong L, Xu Z, An S, Jia X, Zhang W, Jiang X. A glutathione-depleted prodrug platform of $MnO_2$-coated hollow polydopamine nanospheres for effective cancer diagnosis and therapy. New J Chem. 2020;44(19):7838–48.
101. Miao Y, Zhou X, Bai J, Zhao W, Zhao X. Hollow polydopamine spheres with removable manganese oxide nanoparticle caps for tumor microenvironment-responsive drug delivery. Chem Eng J. 2022;430:133089.
102. Cho S, Park W, Kim D-H. Silica-coated metal chelating-melanin nanoparticles as a dual-modal contrast enhancement imaging and therapeutic agent. ACS Appl Mater Inter. 2016;9(1):101–11.
103. Yang Z, Ren J, Ye Z, Zhu W, Xiao L, Zhang L, et al. Bio-inspired synthesis of PEGylated polypyrrole@polydopamine nanocomposites as theranostic agents for $T_1$-weighted MR imaging guided photothermal therapy. J Mater Chem B. 2017;5(5):1108–16.
104. Sun J, Xu W, Li L, Fan B, Peng X, Qu B, et al. Ultrasmall endogenous biopolymer nanoparticles for magnetic resonance/photoacoustic dual-modal imaging-guided photothermal therapy. Nanoscale. 2018;10(22):10584–95.
105. Jiang Q, Liu Y, Guo R, Yao X, Sung S, Pang Z, et al. Erythrocyte-cancer hybrid membrane-camouflaged melanin nanoparticles for enhancing photothermal therapy efficacy in tumors. Biomaterials. 2019;192:292–308.
106. Wang Y, Li T, Ma P, Bai H, Xie Y, Chen M, et al. Simultaneous enhancements of UV-shielding properties and photostability of poly(vinyl alcohol) via incorporation of sepia eumelanin. ACS Sustain Chem Eng. 2016;4(4):2252–8.
107. Fan B, Yang X, Li X, Lv S, Zhang H, Sun J, et al. Photoacoustic-imaging-guided therapy of functionalized melanin nanoparticles: combination of photothermal ablation and gene therapy against laryngeal squamous cell carcinoma. Nanoscale. 2019;11(13):6285–96.
108. Dong Z, Feng L, Hao Y, Chen M, Gao M, Chao Y, et al. Synthesis of hollow biomineralized $CaCO_3$–polydopamine nanoparticles for multimodal imaging-guided cancer photodynamic therapy with reduced skin photosensitivity. J Am Chem Soc. 2018;140(6):2165–78.
109. Li S, Zhang L, Liang X, Wang T, Chen X, Liu C, et al. Tailored synthesis of hollow MOF/polydopamine Janus nanoparticles for synergistic multi-drug chemo-photothermal therapy. Chem Eng J. 2019;378:122175.
110. Lv Z, He S, Wang Y, Zhu X. Noble metal nanomaterials for NIR-triggered Photothermal therapy in Cancer. Adv Healthc Mater. 2021;10(6):2001806.
111. Liu P, Zheng H, Yang Z, Ba L, Zhu W, Lin L, et al. Facile preparation of versatile gadolinium-chelated protein nanocomposite for $T_1$ magnetic resonance imaging-guided photodynamic and photothermal synergetic therapy. J Mater Chem B. 2018;6(11):1688–98.
112. Mo Z, Li Q, Zhao K, Xu Q, Hu H, Chen X, et al. A Nanoarchitectonic approach enables triple modal synergistic therapies to enhance antitumor effects. ACS Appl Mater Inter. 2022;14(8):10001–14.
113. Wu K, Zhao H, Sun Z, Wang B, Tang X, Dai Y, et al. Endogenous oxygen generating multifunctional theranostic nanoplatform for enhanced photodynamic-photothermal therapy and multimodal imaging. Theranostics. 2019;9(25):7697.
114. Yang Z, Zhang L, Wei J, Li R, Xu Q, Hu H, et al. Tumor acidity-activatable photothermal/Fenton nanoagent for synergistic therapy. J Colloid Interface Sci. 2022;612:355–66.
115. Gao H, Chi B, Tian F, Xu M, Xu Z, Li L, et al. Prussian blue modified metal organic frameworks for imaging guided synergetic tumor therapy with hypoxia modulation. J Alloys Compd. 2021;853:157329.
116. Jiang F, Zhao Y, Yang C, Cheng Z, Liu M, Xing B, et al. A tumor microenvironment-responsive co/ZIF-8/ICG/Pt Nanoplatform for Chemodynamic and enhanced photodynamic antitumor therapy. Dalton Trans. 2022;51:2798–804.
117. Du W, Liu T, Xue F, Chen Y, Chen Q, Luo Y, et al. Confined nanoparticles growth within hollow mesoporous nanoreactors for highly efficient MRI-guided photodynamic therapy. Chem Eng J. 2020;379:122251.
118. Yaqoob AA, Ahmad H, Parveen T, Ahmad A, Oves M, Ismail IM, et al. Recent advances in metal decorated nanomaterials and their various biological applications: a review. Front Chem. 2020;8:341.
119. Mushtaq A, Hou Y, Tian C, Deng T, Xu C, Sun Z, et al. Facile synthesis of Mn doped $TiO_2$ rhombic nanocomposites for enhanced $T_1$-magnetic resonance imaging and photodynamic therapy. Mater Res Bull. 2021;144:111481.
120. Zhu W, Liu K, Sun X, Wang X, Li Y, Cheng L, et al. $Mn^{2+}$-doped prussian blue nanocubes for bimodal imaging and photothermal therapy with enhanced performance. ACS Appl Mater Inter. 2015;7(21):11575–82.
121. Zhou R, Sun S, Li C, Wu L, Hou X, Wu P. Enriching Mn-doped ZnSe quantum dots onto mesoporous silica nanoparticles for enhanced fluorescence/magnetic resonance imaging dual-modal bio-imaging. ACS Appl Mater Inter. 2018;10(40):34060–7.
122. Lin L-S, Wang J-F, Song J, Liu Y, Zhu G, Dai Y, et al. Cooperation of endogenous and exogenous reactive oxygen species induced by zinc peroxide nanoparticles to enhance oxidative stress-based cancer therapy. Theranostics. 2019;9(24):7200.
123. Tian F, Liu F, Chen Q, Wang L, Guan S, Zhou S, et al. Revealing Mn doping effect in transition metal phosphides to trigger active centers for highly efficient Chemodynamic and NIR-II Photothermal therapy. Chem Eng J. 2022;435:134780.
124. Fu C, Zhou H, Tan L, Huang Z, Wu Q, Ren X, et al. Microwave-activated Mn-doped zirconium metal–organic framework nanocubes for highly effective combination of microwave dynamic and thermal therapies against cancer. ACS Nano. 2017;12(3):2201–10.
125. Zou R, Li J, Yang T, Zhang Y, Jiao J, Wong K-L, et al. Biodegradable manganese engineered nanocapsules for tumor-sensitive near-infrared persistent luminescence/magnetic resonance imaging and simultaneous chemotherapy. Theranostics. 2021;11(17):8448.
126. Dong S, Dong Y, Liu B, Liu J, Liu S, Zhao Z, et al. Guiding transition metal-doped hollow cerium tandem Nanozymes with elaborately regulated multi-enzymatic activities for intensive Chemodynamic therapy. Adv Mater. 2022;34:2107054.
127. Yan B-B, Xue C-C, Li M-H, Dong L, Zhao Y, Luo Z, et al. All-in-one hollow nanoformulations enabled imaging-guided Mn-amplified chemophototherapy against hepatocellular carcinoma. Nano Today. 2022;43:101382.
128. Ma W, Chen X, Fu L, Zhu J, Fan M, Chen JY, et al. Ultra-efficient antibacterial system based on photodynamic therapy and CO gas therapy for synergistic antibacterial and ablation biofilms. ACS Appl Mater Inter. 2020;12(20):22479–91.
129. Wu J, Meng Z, Exner AA, Cai X, Xie X, Hu B, et al. Biodegradable cascade nanocatalysts enable tumor-microenvironment remodeling for controllable CO release and targeted/synergistic cancer nanotherapy. Biomaterials. 2021;276:121001.
130. Zheng S, Dou P, Jin S, Jiao M, Wang W, Jin Z, et al. Tumor microenvironment/NIR-responsive carbon monoxide delivery with hollow mesoporous CuS nanoparticles for MR imaging guided synergistic therapy. Mater Design. 2021;205:109731.
131. Zhang L, Forgham H, Shen A, Qiao R, Guo B. Recent Advances in Single Fe-Based Nanoagents for Photothermal–Chemodynamic Cancer Therapy. Biosensors. 2022;12(2):86.
132. Shi Y, Zhang J, Huang H, Cao C, Yin J, Xu W, et al. Fe-doped Polyoxometalate as acid-aggregated Nanoplatform for NIR-II Photothermal-enhanced Chemodynamic therapy. Adv Healthc Mater. 2020;9(9):2000005.
133. Xu H, Yu N, Zhang J, Wang Z, Geng P, Wen M, et al. Biocompatible Fe-Hematoporphyrin coordination nanoplatforms with efficient sonodynamic-chemo effects on deep-seated tumors. Biomaterials. 2020;257:120239.
134. Leonel AG, Mansur AA, Carvalho SM, Outon LEF, Ardisson JD, Krambrock K, et al. Tunable magnetothermal properties of cobalt-doped magnetite–carboxymethylcellulose ferrofluids: smart nanoplatforms

for potential magnetic hyperthermia applications in cancer therapy. Nanoscale Adv. 2021;3(4):1029–46.
135. Han H, Xu X, Kan H, Tang Y, Liu C, Wen H, et al. Synergistic photodynamic/photothermal bacterial inactivation over heterogeneous quaternized chitosan/silver/cobalt phosphide nanocomposites. J Colloid Interface Sci. 2022;616:304–15.
136. Wu Y, Song X, Xu W, Ky S, Wang Z, Lv Z, et al. NIR-activated multimodal Photothermal/Chemodynamic/magnetic resonance imaging Nanoplatform for anticancer therapy by Fe(II) ions doped MXenes (Fe-$Ti_3C_2$). Small. 2021;17(33):2101705.
137. Chen Y, Gao M, Zhang L, Ha E, Hu X, Zou R, et al. Tumor microenvironment responsive biodegradable Fe-doped $MoO_x$ nanowires for magnetic resonance imaging guided Photothermal-enhanced Chemodynamic synergistic antitumor therapy. Adv Healthc Mater. 2021;10(6):2001665.
138. Zhao L, Yang Q, Guo W, Zhang F, Yu K, Yang C, et al. Non-stoichiometric cobalt sulfide nanodots enhance photothermal and chemodynamic therapies against solid tumor. J Colloid Interface Sci. 2021;600:390–402.
139. Zuo W, Liu N, Chang Z, Liu J, Jin Q, Chen L, et al. Single-site bimetallic nanosheet for imaging guided mutually-reinforced photothermal-chemodynamic therapy. Chem Eng J. 2022;442:136125.
140. Ren Q, Yang K, Zou R, Wan Z, Shen Z, Wu G, et al. Biodegradable hollow manganese/cobalt oxide nanoparticles for tumor theranostics. Nanoscale. 2019;11(47):23021–6.
141. Guan S, Liu X, Fu Y, Li C, Wang J, Mei Q, et al. A biodegradable "Nanodonut" for magnetic resonance imaging and enhanced chemo/photothermal/chemodynamic therapy through responsive catalysis in tumor microenvironment. J Colloid Interface Sci. 2022;608:344–54.
142. Xu M, Gao H, Ji Q, Chi B, He L, Song Q, et al. Construction multifunctional nanozyme for synergistic catalytic therapy and phototherapy based on controllable performance. J Colloid Interface Sci. 2022;609:364–74.
143. Jiang F, Yang C, Ding B, Liang S, Zhao Y, Cheng Z, et al. Tumor microenvironment-responsive $MnSiO_3$-Pt@BSA-Ce6 nanoplatform for synergistic catalysis-enhanced sonodynamic and chemodynamic cancer therapy. Chin Chem Lett. 2022;33(6):2959–64. https://doi.org/10.1016/j.cclet.2021.12.096.
144. Chen J, Zhang W, Zhang M, Guo Z, Wang H, He M, et al. Mn(II) mediated degradation of artemisinin based on $Fe_3O_4$@$MnSiO_3$-FA nanospheres for cancer therapy *in vivo*. Nanoscale. 2015;7(29):12542–51.
145. Sun X, Zhang G, Du R, Xu R, Zhu D, Qian J, et al. A biodegradable $MnSiO_3$@$Fe_3O_4$ nanoplatform for dual-mode magnetic resonance imaging guided combinatorial cancer therapy. Biomaterials. 2019;194:151–60.
146. Gao P, Pan W, Li N, Tang B. Boosting cancer therapy with organelle-targeted nanomaterials. ACS Appl Mater Inter. 2019;11(30):26529–58.
147. Ma X, Gong N, Zhong L, Sun J, Liang X-J. Future of nanotherapeutics: targeting the cellular sub-organelles. Biomaterials. 2016;97:10–21.
148. Chen WH, Luo GF, Zhang XZ. Recent advances in subcellular targeted cancer therapy based on functional materials. Adv Mater. 2019;31(3):1802725.
149. Wang R, Li X, Yoon J. Organelle-targeted photosensitizers for precision photodynamic therapy. ACS Appl Mater Inter. 2021;13(17):19543–71.
150. Ma W, Zhang H, Li S, Wang Z, Wu X, Yan R, et al. A multifunctional Nanoplatform based on Fenton-like and Russell reactions of cu, Mn bimetallic ions synergistically enhanced ROS stress for improved Chemodynamic therapy. ACS Biomater Sci Eng. 2022;8(3):1354–66.
151. Tang Q, Yu Y-T, Zhang H-L, Wang Y, Liu J, Yang S-P, et al. NIR light-controlled mitochondria-targeted delivery of carbon monoxide combined with histone deacetylase inhibition for synergistic anticancer therapy. J Inorg Biochem. 2022;226:111656.
152. Xu J, Shamul JG, Kwizera EA, He X. Recent advancements in mitochondria-targeted nanoparticle drug delivery for Cancer therapy. Nanomaterials. 2022;12(5):743.
153. Lv J, Wang S, Qiao D, Lin Y, Hu S, Li M. Mitochondria-targeting multifunctional nanoplatform for cascade phototherapy and hypoxia-activated chemotherapy. J Nanobiotechnol. 2022;20(1):1–16.
154. Guo J, Tan D, Lou C, Guo S, Jin X, Qu H, et al. A tumor-penetrable drug nanococktail made from human histones for interventional nucleus-targeted chemophotothermal therapy of drug-resistant tumors. Bioact Mater. 2022;9:554–65.
155. Wang H, Zhang H, Xiang Y, Pan W, Li N, Tang B. An efficient strategy for cancer therapy using a tumor-and lysosome-targeted organic photothermal agent. Nanoscale. 2021;13(19):8790–4.

## Publisher's Note